1

Introduction to Lanthanide Ion Luminescence

Ana de Bettencourt-Dias

Department of Chemistry, University of Nevada, USA

1.1 History of Lanthanide Ion Luminescence

After the isolation of a sample of yttrium oxide from a new mineral by Johan Gadolin in 1794, several of the lanthanides, namely praseodymium and neodymium, as well as cerium, lanthanum, terbium and erbium were isolated in different degrees of purity [1]. It was only after Kirchhoff and Bunsen introduced the spectroscope in 1859 as a means of characterising elements that the remaining lanthanides were discovered and the already known ones could be obtained in pure form [2]. Spark spectroscopy provided the means to finally isolate in pure form the remaining lanthanides [3–5]. As will be discussed below, the 4*f* valence orbitals are buried within the core of the ions, shielded from the coordination environment by the filled 5*s* and 5*p* orbitals, and do not experience significant coupling with the ligands. Therefore, the electronic levels of the ions can be described in an analogous way to the atomic electronic levels with a Hamiltonian in central field approximation with electrostatic Coulomb interactions, spin–orbit coupling and finally crystal field and Zeeman effects added as perturbations. All these perturbations lead to a lifting of the degeneracy of the electronic levels and transitions between these split levels are experimentally observed [6]. These transitions, however, are forbidden by the parity rule, as there is no change in parity between excited and ground state. That the emission was nonetheless seen puzzled scientists for a long time [7]. Only when Judd and Ofelt independently proposed their theory of induced electric dipole

Luminescence of Lanthanide Ions in Coordination Compounds and Nanomaterials, First Edition.
Edited by Ana de Bettencourt-Dias.

transitions [8,9] could the appearance of these transitions be satisfactorily explained. As the transitions are forbidden, the direct excitation of the lanthanide ions is also not easily accomplished, and this is why sensitised emission is a more appealing and energy efficient way to promote lanthanide-centred emission. While the ability of the lanthanide salts to emit light was key to their isolation in pure form, sensitised emission was first described by S.I. Weissman only in 1942 [10]. This author realised that when complexes of Eu(III) with salicylaldehyde and benzoylacetonato, as well as other related ligands, were irradiated with light in the wavelength range in which the organic ligands absorb, strong europium-characteristic red emission ensued. Weissman further observed that the emission intensity was temperature and solvent dependent, as opposed to what is seen for europium nitrate solutions [10]. After this seminal work, interest in sensitised luminescence spread through the scientific community, as the potential application of lanthanides for imaging and sensing was quickly recognised [11,12].

1.2 Electronic Configuration of the +III Oxidation State

1.2.1 The 4*f* Orbitals

The lanthanides' position in the fourth period as the inner transition elements of the periodic table indicates that the filling of the 4*f* valence orbitals commences with them. The electronic configuration of the lanthanides is $[Xe]4f^n6s^2$, with notable exceptions for lanthanum, cerium, gadolinium and lutetium, which have a $[Xe]4f^{n-1}5d^16s^2$ configuration. Upon ionisation to the most common +III oxidation state, the configuration is uniformly $[Xe]4f^{n-1}$. La(III) therefore does not possess any *f* electrons, while Lu(III) has a filled 4*f* orbital. While the 4*f* orbitals are the valence orbitals, they are shielded from the coordination environment by the filled 5*s* and 5*p* orbitals, which are more spatially extended, as shown in Fig. 1.1, which displays the radial charge density distribution for Pr(III) [13]. Therefore, lanthanides bind mostly through ionic interactions and the ligand field perturbation upon the 4*f* orbitals is minimal. Nonetheless, as will be discussed below, symmetry considerations imposed by the ligand field affect the emission spectra of the lanthanide ions.

1.2.2 Energy Level Term Symbols

It is usual to describe the configurations of hydrogen-like atoms or ions, that is with only one electron, in terms of the quantum numbers n, l, m_l, s and m_s. In polyelectronic atoms and ions, exchange and pairing energies lead to different configurations, or microstates, with different energies, which are described by new quantum numbers, the total orbital angular momentum quantum number L and its projection along the z axis, the total magnetic orbital angular momentum M_L, and the total spin angular momentum quantum number S, often indicated as the spin multiplicity, $2S+1$, as well as its projection along the z axis, the total magnetic spin quantum number M_S. In the case of heavy elements, such as lanthanides, coupling of the spin and angular momenta is seen, and an additional quantum number, J, the spin–orbit coupling or Russell–Saunders quantum number, is commonly utilised. As will be mentioned below, intermediate coupling for lanthanides is more correct, but the

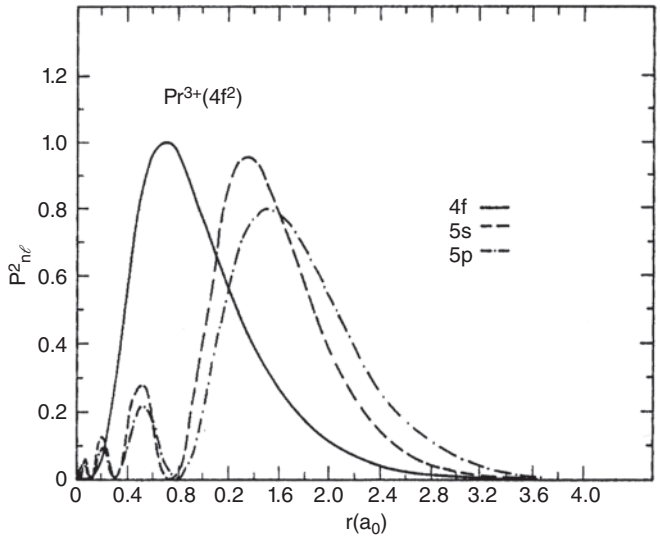

Figure 1.1 *Radial charge density distribution of Pr(III). Reproduced from [13] with permission from Elsevier*

Russell–Saunders formalism is simple to use and will be carried through this chapter. Term symbols with the format $^{2S+1}L_J$, which summarise the quantum number information, are assigned to describe the individual microstates. For a polyelectronic atom or ion with i electrons,

$$L = \sum_i l_i, \quad M_L = -L, \ldots, L$$

$$S = \sum_i s_i, \quad s_i = 1/2$$

and

$$J = L + S, L + S - 1, \ldots, |L - S|.$$

Term symbols can be obtained by determining the microstates, or allowed combinations of all electrons described by quantum numbers, of the atom or ion under consideration and methods to do it is can be found in textbooks [14,15]. Since multiple combinations of electrons are allowed, and therefore many microstates are present, Hund's rules are followed for determination of the ground state. The ground state will have the largest spin multiplicity and the largest orbital multiplicity corresponding to the largest value of L. Finally, if S and L are equal for two states, the ground state will correspond to the largest value of J, if the electron shell is more than half-filled, or an inverted multiplet and the smallest value of J, if the orbital is less than half-filled, which is a regular multiplet. The ground state term symbols for f^n ($n =$ number of electrons in the f shell) configurations are shown in Table 1.1.

Table 1.1 *Ground state term symbols for* f^n *electronic configurations*

Configuration	Term
f^0/f^{14}	$^1S_0$
f^1/f^{13}	$^2F_{5/2}/^2F_{7/2}$
f^2/f^{12}	$^3H_4/^3H_6$
f^3/f^{11}	$^4I_{9/2}/^4I_{15/2}$
f^4/f^{10}	$^5I_4/^5I_8$
f^5/f^9	$^6H_{5/2}/^6H_{15/2}$
f^6/f^8	$^7F_0/^7F_6$
f^7	$^8S_{7/2}$

A complete diagram, showing the ground and excited states of all lanthanide ions in the +III oxidation state with corresponding term symbols, is displayed in Fig. 1.2.

Table 1.2 summarises the most commonly observed emission transitions for the emissive Ln(III) ions.

Table 1.2 *Most common emissive f-f transitions of* Ln^{3+} *[16–28]*

Ln	Transition	λ [nm]
Pr	$^1D_2 \rightarrow {}^3F_4$	1000
	$^1D_2 \rightarrow {}^1G_4$	1440
	$^1D_2 \rightarrow {}^3H_J (J = 4, 5)$	600, 690
	$^3P_0 \rightarrow {}^3H_J (J = 4 - 6)$	490, 545, 615, 640,
	$^3P_0 \rightarrow {}^3F_J (J = 2 - 4)$	700, 725
Nd	$^4F_{3/2} \rightarrow {}^4I_J (J = 9/2 - 13/2)$	900, 1060, 1350
Sm	$^4G_{5/2} \rightarrow {}^6H_J (J = 5/2 - 13/2)$	560, 595, 640, 700, 775
	$^4G_{5/2} \rightarrow {}^6F_J (J = 1/2 - 9/2)$	870, 887, 926, 1010, 1150
Eu	$^5D_0 \rightarrow {}^7F_J (J = 0 - 6)$	580, 590, 615, 650, 720, 750, 820
Gd	$^6P_{7/2} \rightarrow {}^8S_{7/2}$	315
Tb	$^5D_4 \rightarrow {}^7F_J (J = 6 - 0)$	490, 540, 580, 620, 650, 660, 675
Dy	$^4F_{9/2} \rightarrow {}^6H_J (J = 15/2 - 9/2)$	475, 570, 660, 750
	$^4I_{15/2} \rightarrow {}^6H_J (J = 15/2 - 9/2)$	455, 540, 615, 695
Ho	$^5S_2 \rightarrow {}^5I_J (J = 8, 7)$	545, 750
	$^5F_5 \rightarrow {}^5I_J (J = 8, 7)$	650, 965
Er	$^4S_{3/2} \rightarrow {}^4I_J (J = 15/2, 13/2)$	545, 850
	$^4F_{9/2} \rightarrow {}^4I_{15/2}$	660
	$^4I_J (J = 9/2, 13/2) \rightarrow {}^4I_{15/2}$	810, 1540
Tm	$^1D_2 \rightarrow {}^3F_4, {}^3H_4, {}^3F_J (J = 3, 2)$	450, 650, 740, 775
	$^1G_4 \rightarrow {}^3H_6, {}^3F_4, {}^3H_5$	470, 650, 770
	$^3H_4 \rightarrow {}^3H_6$	800
Yb	$^2F_{5/2} \rightarrow {}^2F_{7/2}$	980

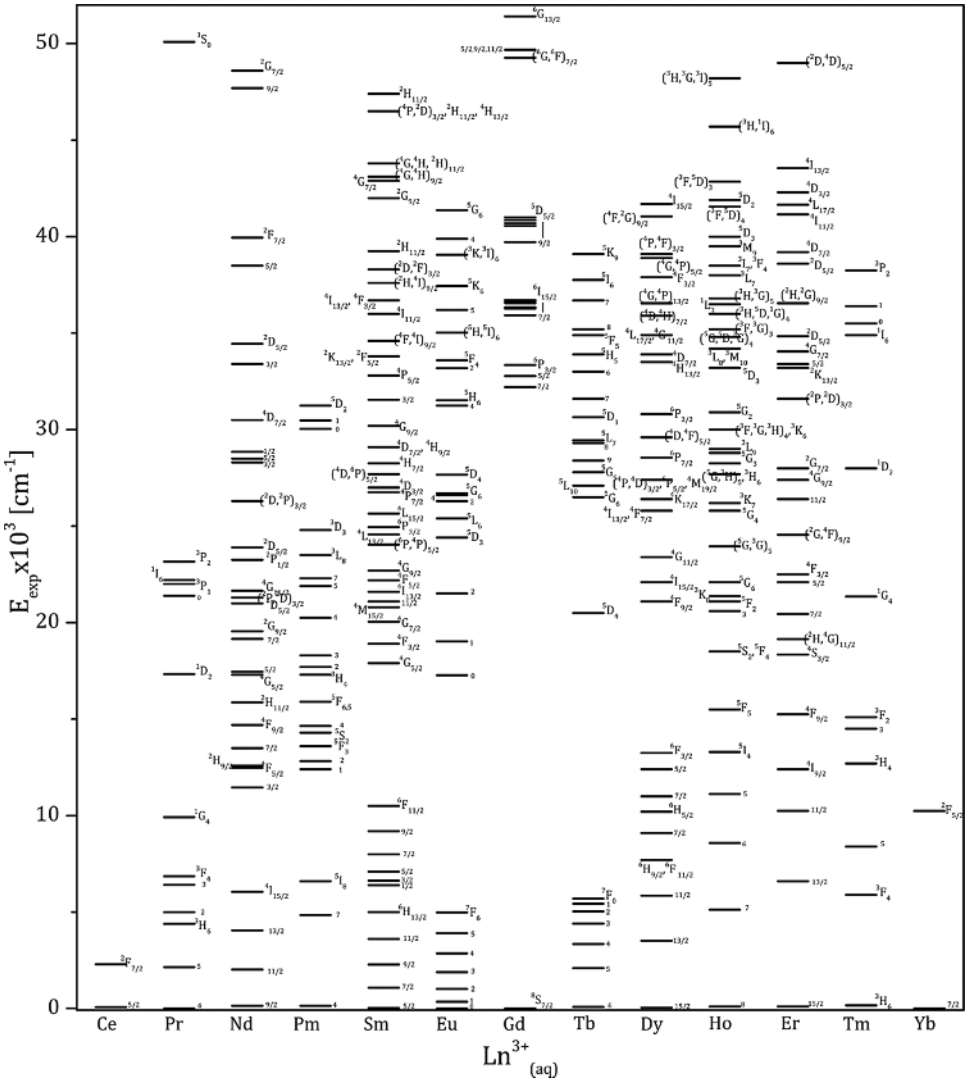

Figure 1.2 *Diagram of energy levels with corresponding term symbols for Ln(III) [16]*

1.3 The Nature of the *f-f* Transitions

1.3.1 Hamiltonian in Central Field Approximation and Coulomb Interactions

The behaviour of an electron is described by the wave function ψ, which is a solution of the Schrödinger equation 1.1.

$$H\psi = E\psi \tag{1.1}$$

This equation only has an exact solution for systems with one electron, but for polyelectronic systems with N electrons, the solution can be approximated by considering that each

electron is moving independently in a central spherically symmetric field $U(r_i)/e$ of the averaged potentials of all other electrons [6]. The Hamiltonian H_{CFA} for this central field approximation is shown in Equation 1.2.

$$H_{CFA} = \sum_{i=1}^{N} \left[\frac{-\hbar^2}{2m} \nabla^2 + U(r_i) \right] \tag{1.2}$$

$\hbar$ is the reduced Planck constant, m the mass and the Laplace operator is given by Equation 1.3.

$$\nabla^2 = \frac{\partial^2}{\partial x^2} + \frac{\partial^2}{\partial y^2} + \frac{\partial^2}{\partial z^2} \tag{1.3}$$

The Schrödinger equation can thus be written as shown in Equation 1.4.

$$\sum_{i=1}^{N} \left[\frac{-\hbar^2}{2m} \nabla^2 + U(r_i) \right] \Psi = E_{CFA} \Psi \tag{1.4}$$

In the central field approximation, solutions can be chosen such that the overall wavefunction and energy of the system are sums of wavefunctions and energies of one-electron systems, as shown in Equation 1.5.

$$\Psi = \sum_{i=1}^{N} \psi_i(a^i) \tag{1.5a}$$

$$E_{CFA} = \sum_{i=1}^{N} E_i \tag{1.5b}$$

a^i stands for the quantum numbers n, l and m_l which describe the state of the electron in the central field. By introducing the polar coordinates r, θ and ϕ instead of the Cartesian coordinates x, y and z, one can separate each one-electron wave function into its radial R_{nl} and angular Y_{lm_l} components, as shown in Equation 1.6.

$$\psi_i(a^i) = \frac{1}{r} R_{nl}(r) Y_{lm_l}(\theta, \phi) \tag{1.6}$$

Since R_{nl} is a function of r only, it depends on the central field potential $U(r_i)$. A solution to this wave function, shown in Equation 1.7, is approximated and depends on the form of the central field.

$$R_{nl}(r) = -\left[\left(\frac{2Z}{na_0} \right)^3 \frac{(n-l-1)!}{2n\{n+l\}^3} \right]^{1/2} e^{-\frac{\rho}{2}} \rho^l L_{n+l}^{2l+1}(\rho) \tag{1.7}$$

with $\rho = \frac{2Z}{na_0} r$ and $a_0 = \frac{\hbar^2}{4\pi^2 \mu e^2}$, where a_0 is the Bohr radius and μ the reduced mass. This expression also includes the Laguerre polynomials $L_{n+l}^{2l+1}(\rho)$ shown in Equation 1.8.

$$L_{n+l}^{2l+1}(\rho) = \sum_{k=0}^{n-l-1} (-1)^{k+1} \frac{\{(n+l)!\}^2}{(n-l-1-k)!(2l+1+k)!k!} \rho^k \tag{1.8}$$

The angular wave functions, which are Laplacian spherical harmonics, on the other hand, are similar to the one-electron wave function and can thus be solved. Their expression is given in Equation 1.9.

$$Y_{lm_l}(\theta, \phi) = (-1)^m \left[\frac{(2l+1)(l-|m_l|)!}{4\pi(l+|m_l|)!} \right]^{\frac{1}{2}} P_l^{m_l}(\cos\theta) e^{im_l\phi} \tag{1.9}$$

$P_l^{m_l}(\cos\theta)$ are the Legendre functions shown in Equation 1.10.

$$P_l^{m_l}(\cos\theta) = \frac{(1-\cos^2\theta)^{m_l/2}}{2^l l!} \frac{d^{m_l+l}}{d\cos^{m_l+l}\theta} (\cos^2\theta - 1)^l \tag{1.10}$$

Relativistic corrections to the Schrödinger equation lead to the introduction of a spin function $\delta(m_s, \sigma)$, where σ is a spin coordinate and m_s is the magnetic spin quantum number, to the one electron wave function in Equation 1.6, which then takes the shape shown in Equation 1.11.

$$\psi(n, l, m_l, m_s) = \delta(l, n, m_l, m_s) R_{nl}(r) Y_{lm_l}(\theta, \phi) \tag{1.11}$$

Equation 1.5a can now be rewritten as Equation (1.12).

$$\Psi = \sum_{i=1}^{N} \psi_i(\alpha^i) \tag{1.12}$$

While the two equations look similar, in Equation 1.12 α^i stands for the four quantum numbers n, l, m_l and m_s, which describe the state of each i of the N electrons. These permutate to generate equally valid states following Pauli's exclusion principle, to yield anti-symmetric wave functions in the central field, which are solutions to the Schrödinger equation (Equation 1.4).

The lack of perturbations to the Hamiltonian in the central field approximation results in high degeneracy D (Equation 1.13) of the f electron configurations.

$$D = \frac{(4l+2)!}{N!(4l+2-N)!} = \frac{14!}{N!(14-N)!} \qquad \text{for } l = 3 \tag{1.13}$$

The Hamiltonian for the perturbation introduced by the potential energy H_{pot} felt by all electrons in the field of the nucleus corrected for the central spherically symmetric field is given by Equation 1.14.

$$H_{pot} = \sum_{i=1}^{N} \left[-\frac{Ze^2}{r_i} - U(r_i) \right] \tag{1.14}$$

Ze is the nuclear charge, r_i the position coordinates of electron i and $U(r_i)$ the spherical repulsive potential of all other electrons experienced by electron i moving independently in the field of the nucleus.

The repulsive Coulomb energy between pairs of electrons is an important perturbation to the central field approximation and its Hamiltonian $H_{Coulomb}$ is given by Equation 1.15.

$$H_{Coulomb} = \sum_{i<j}^{N} \frac{e^2}{r_{ij}} \tag{1.15}$$

e is the charge of the electron and r_{ij} is the distance between electrons i and j.

By applying $H_{Coulomb}$ to the wave function of the unperturbed system, it can be shown that the electrostatic repulsion energy E_{ER} of the system is given by Equation 1.16.

$$E_{ER} = \sum_{k=2,4,6} f_k F^k \tag{1.16}$$

Here, k is an integer of values 2, 4 and 6, f_k are the coefficients representing the angular part of the wave function [29] and F^k are the electrostatic Slater two-electron radial integrals given by Equation 1.17.

$$F^k = (4\pi)^2 e^2 \int_0^\infty \int_0^\infty \frac{r_<^k}{r_>^{k+1}} R_{nl}^2(r_i) R_{n'l'}^2(r_j) r_i^2 r_j^2 dr_i dr_j \tag{1.17}$$

$r_<$ is the smaller and $r_>$ the larger of the values of r_i and r_j. F_k instead of the Slater integrals are often indicated, for which:

$$F_2 = F^2/225$$
$$F_4 = F^4/1089$$
$$F_6 = F^6/7361.64$$

In the case of hydrogenic wave functions the following relationships are valid [30].

$$F_4 = 0.145\, F_2 \qquad F_6 = 0.0164\, F_2$$

These show that the values of F_k decrease as k increases. Values of F_2 for the configurations f^2 to f^{13} are tabulated in Table 1.3 and show that they increase with increasing atomic number, as the inter-electronic repulsion is expected to increase.

The f_k angular coefficients are hydrogen-like and can be determined from

$$f_k = \frac{(2l+1)(l-|m_l|)!}{2(l+|m_l|)!} \frac{(2l'+1)(l'-|m_l'|)!}{2(l'+|m_l'|)!} \int_0^\pi \{P_l^{m_l}(\cos\theta_i)\}^2 P_0^k(\cos\theta_i) \sin\theta_i d\theta_i \times \int_0^\pi \{P_{l'}^{m_{l'}}(\cos\theta_i)\}^2 P_0^k(\cos\theta_i) \sin\theta_i d\theta_i \tag{1.18}$$

As above, $P_l^{m_l}$, $P_{l'}^{m_{l'}}$ and P_0^k are Legendre polynomials.

Table 1.3 *Comparison of the average magnitude of perturbations for transition metal and lanthanide ions in cm^{-1} [13]*

Valence configuration	$H_{Coulomb}$	H_{s-o}	H_{cf}
$3d^N$	70 000	500	15 000
$4d^N$	50 000	1000	20 000
$5d^N$	20 000	2000	25 000
$4f^N$	70 000	1500	500
$5f^N$	50 000	2500	2000

In addition to the Coulomb interactions of electron–electron repulsion and electron–nucleus attraction, further perturbations influence the energy levels of the lanthanide ions, such as the coupling of the spin and angular momenta, commonly designated spin–orbit coupling, the crystal field or Stark effect, and the interaction with a magnetic field or Zeeman effect, which will be described in the following sections.

As illustrated in Fig. 1.3, by comparison to electron–electron repulsion, which leads to energy splits on the order of $10^4\,cm^{-1}$, and spin–orbit coupling, with splits on the order of $10^3\,cm^{-1}$, the crystal field and Zeeman effects are small perturbations, resulting in energy level splitting on the order of $10^2\,cm^{-1}$ at the most [13]. The magnitude of these data compared to the *d* metals is shown comparatively in Table 1.4. In the case of transition metals, the crystal field splitting dominates the spin–orbit coupling. However, for lanthanide ions, the crystal field splitting is almost negligible. The spin–orbit coupling is of increasing

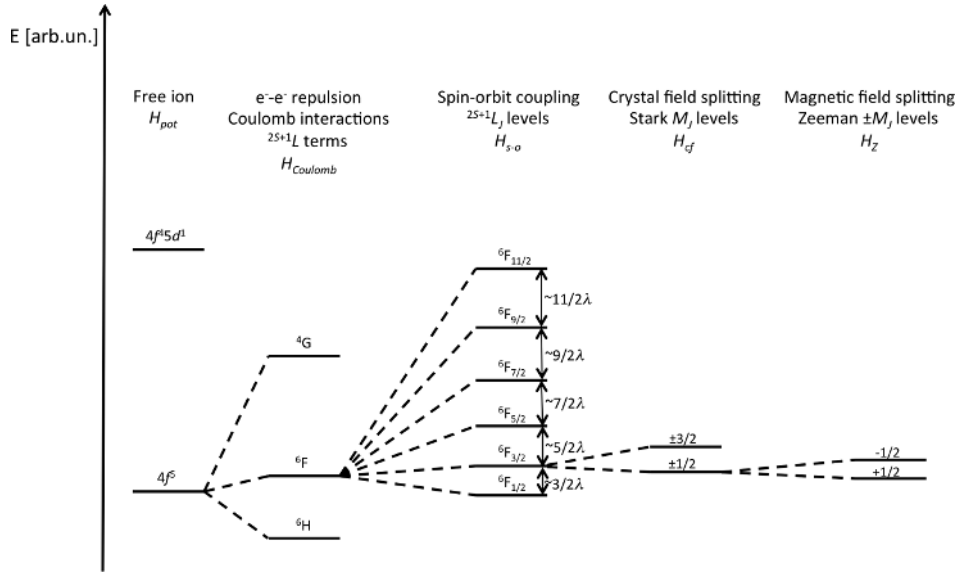

Figure 1.3 *Effect of the perturbations [Coulomb ($H_{Coulomb}$), spin–orbit (H_{s-o}), crystal field (H_{cf}), and magnetic field (H_Z)] on the electron configuration of an arbitrary Ln(III) Kramers' ion. Energy units are arbitrary and not to scale. λ is described in Section 3.2*

Table 1.4 *Spin–orbit radial integral ζ_{nl}, spin-orbit coupling constant λ and F_2 values for the $Ln^{3+}_{(aq)}$ ions [25–28,31]*

f^N	ζ_{nl} [cm^{-1}]	λ [cm^{-1}][a]	F_2 [cm^{-1}][b]
f^1	625	625	
f^2	740	370	305
f^3	884	295	321
f^4	1022	250	338
f^5	1157	231	364
f^6	1326	221	369
f^7	1450	0	384
f^8	1709	−285	401
f^9	1932	−386	407
f^{10}	2141	−535	419
f^{11}	2380	−793	440
f^{12}	2628	−1314	461
f^{13}	2870	−2880	444[c]

[a] f^1 as Ce:$LaCl_3$ [32] and f^{13} as $Yb_3Ga_5O_{12}$ [33].
[b] [16]
[c] [30]

importance for the heavier elements. However, in the case of the lanthanides, it is still approximately an order of magnitude smaller than the Coulomb interactions and one order of magnitude larger than the crystal field splitting; therefore an intermediate coupling scheme, in which *j-j* in addition to Russell–Saunders coupling is also important, is more correct. Nonetheless, as mentioned above, the latter formalism is utilised due to its simplicity.

1.3.2 Spin–Orbit Coupling

The spin and angular momenta of the individual electrons couple with each other and this coupling is increasingly important with atomic number. The Hamiltonian $H_{s\text{-}o}$ that describes this perturbation is given in Equation 1.19.

$$H_{s\text{-}o} = \sum_{i=1}^{N} \xi(r_i)(s_i \cdot l_i) \tag{1.19}$$

r_i is the position coordinate of electron i, and s_i and l_i are its spin and angular momentum quantum numbers. $\xi(r_i)$, the single electron spin–orbit coupling constant, is given by Equation 1.20.

$$\xi(r_i) = \frac{\hbar^2}{2m^2c^2r_i}\frac{dU(r_i)}{dr_i} \tag{1.20}$$

In this equation, c is the speed of light in a vacuum and $\hbar$ is the reduced Planck constant. $\xi(r_i)$ is related to the spin–orbit radial integral ζ_{nl} by equation 1.21.

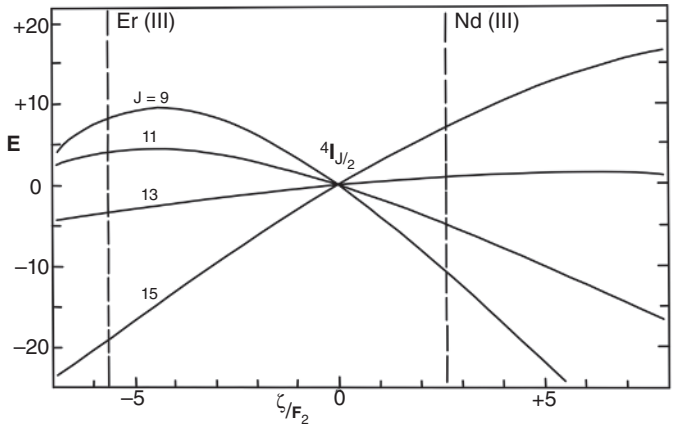

Figure 1.4 *The energies and splitting of the ^4I level for the f^3 and f^{11} configurations as a function of the ratio ζ_{nl}/F_2. The energy levels for the ratios −5.7 for Er(III) and 2.6 for Nd(III) are indicated by the dashed vertical lines. Adapted with permission from [16]. Interscience Publishers: New York, 1968*

$$\zeta_{nl} = \int_0^\infty R_{nl}^2 \xi(r) dr \tag{1.21}$$

and to the many electron spin–orbit coupling constant λ by Equation 1.22, for $S \neq 0$.

$$\lambda = \pm \frac{\xi(r)}{2S} \tag{1.22}$$

Values of ζ_{nl} and λ for the hydrated Ln^{3+} ions are summarised in Table 1.4, with λ positive for a more than half-filled shell and negative for a less than half-filled shell. It can be seen that ζ_{nl} increases with increasing number of f electrons, which corresponds to a higher atomic number Z and a stronger spin–orbit interaction, as expected.

$H_{s\text{-}o}$ will permit coupling of ^{2S+1}L states for $\Delta S \leq 1$ and $\Delta L \leq 1$. This effect is shown in Fig. 1.4, in which the energy splitting of the ^4I level due to spin–orbit coupling is shown as a function of the ratio ζ_{nl}/F_2. The increased curvature of the levels shows the increasing spin–orbit coupling. The energy levels of the reverse multiplet of Er(III) and of the multiplet of Nd(III) are indicated by the vertical dashed lines.

The calculated compositions of the ^4I multiplet levels of Nd(III) and of Er(III) are given below.

Nd(III)	Er(III)
$\langle {}^4I_{9/2} \vert = -0.166[{}^2H] + 0.984[{}^4I]$	$\langle {}^4I_{15/2} \vert = 0.982[{}^4I] - 0.186[{}^2K]$
$\langle {}^4I_{11/2} \vert = 0.995[{}^4I]$	$\langle {}^4I_{13/2} \vert = 0.995[{}^4I]$
$\langle {}^4I_{13/2} \vert = -0.993[{}^4I]$	$\langle {}^4I_{11/2} \vert = 0.133[{}^4G] - 0.129[{}^2H] + 0.442[{}^2H'] + 0.875[{}^4I]$
$\langle {}^4I_{15/2} \vert = 0.993[{}^4I] + 0.118[{}^2K]$	$\langle {}^4I_{9/2} \vert = -0.416[{}^4F] - 0.342[{}^2G] + 0.276[{}^2G'] - 0.219[{}^2H] + 0.438[{}^2H'] + 0.627[{}^4I]$

Here, $\langle {}^4I_J|$ is the wave function of the spin–orbit perturbed state and $[{}^4I]$ is the wave function of the unperturbed state; a state indicated by ' is a state with the same L and S but higher energy. Er(III), the heavier lanthanide ion, experiences a larger spin–orbit coupling, as can be seen from the graph as well as composition of the levels above. It can further be inferred that spin–orbit coupling leads to a splitting of the levels into terms with different J values. Diagonalisation of the energy matrix $\langle l^n \alpha LSJ | \sum_i \xi(r_i) s_i l_i | l^n \alpha' L' S' J' \rangle$ allows estimation of the energies of the split terms (Equation 1.23).

$$\langle l^n \alpha LSJ | \sum_i \xi(r_i) s_i l_i | l^n \alpha' L' S' J' \rangle = (-1)^{L+S'+j} \zeta_{nl} \sqrt{(2l+1)(l+1)} \delta_{JJ'} \times \begin{Bmatrix} L & S & J \\ S' & L' & 1 \end{Bmatrix} \langle l^n \alpha LS || V^{11} || l^n \alpha' L' S' \rangle \tag{1.23}$$

δ_{ij} are the Kronecker delta symbols, for which $\delta_{ij} = 0$ for $i \neq j$ and $\delta_{ij} = 1$ for $i = j$. α stands for all additional quantum numbers which describe the initial and final states of l^n. The doubly reduced matrix elements $\langle l^n \alpha LS || V^{11} || l^n \alpha' L' S' \rangle$, containing the spin–orbit operator V^{11}, are tabulated [34]. The term between curly brackets is the six-j symbol, which describes the coupling of three momenta, in this case L, S and J. Online calculators are available to determine these, or they are tabulated [35]. From the 6-j symbol selection rules arise, as it is only non-zero when:

$$\Delta S = 0, \pm 1 \quad \Delta L = 0, \pm 1$$
$$S' + S \geq 1 \quad L' + L \geq 1$$
$$\Delta J = 0$$

The energy of each term with respect to the barycentre of the parent term ${}^{2S+1}L$ can be approximated by Equation 1.24.

$$E_J = {}^1/_2 \lambda [J(J+1) - L(L+1) - S(S+1)] \tag{1.24}$$

Using this equation, it is possible to estimate that the ${}^3H_5$ energy level of Pr^{3+} ($4f^2$) will be located approximately 370 cm^{-1} or -1λ below the barycentre of the ${}^3H$ level, while the ${}^3H_6$ will be 6λ or 2220 cm^{-1} above and the ${}^3H_4$ level -5λ or 1850 cm^{-1} below [16]. From Equation 1.24 it can further be concluded that the energy gap ΔE between two adjacent levels with $J' = J + 1$ is approximated by Landé's interval rule (see also Fig. 1.3), given in Equation 1.25.

$$\Delta E = \lambda J' \tag{1.25}$$

Landé's interval rule is only strictly obeyed in the case of strong LS coupling and is only approximated in lanthanides, where intermediate coupling, consisting of interaction of levels with the same J but different L and S, is more correct. As a consequence, the magnitude of the interval ΔE determined through Equation 1.25 is usually more accurate for the lower energy levels of the lighter lanthanides. Nonetheless, a good approximation between the experimentally observed gaps and the gaps calculated by Landé's rule is

usually seen, especially for ground-state multiplets. In the case of Pr^{3+} the free ion energy levels for $^3H_4$, $^3H_5$ and $^3H_6$ are located at 0, 2152 and 4389 cm^{-1}, respectively [16], leading to ΔE values of 2152 and 2237 cm^{-1} between $J = 4$ and 5 and $J = 5$ and 6, which reasonably approximate the values of 1850 and 2220 cm^{-1} obtained through Equation 1.25.

1.3.3 Crystal Field or Stark Effects

When lanthanide ions are in inorganic lattices or compounds in general, in addition to the Coulomb interactions and the spin–orbit coupling, each electron i also feels the effect of the crystal field generated by the ligands surrounding the metal ion, in analogy to the effect first described by Stark of an electric field on the lines of the hydrogen spectrum [36]. This perturbation lifts the $2J + 1$ degeneracy and generates new levels with M_J quantum numbers. Since a potential is generated by the electrons of the N ligands, which is felt by the electrons of the lanthanide ions, the Hamiltonian can be defined by Equation 1.26.

$$H_{cf} = -e \sum_1^N V(r_i) \tag{1.26}$$

e is the elementary charge, $V(r_i)$ is the potential felt by electron i and r_i its position. Following the same reasoning utilised to derive Equations 1.6 and 1.12 one can express the Hamiltonian as a function of the crystal field parameters B_q^k, which are related to the spherical harmonics Y_q^k, as shown in Equation 1.27 [37].

$$H_{cf} = \sum_{i,j,k} \left(B_q^k\right)(C_q^k)_i \tag{1.27}$$

The relationships between B_q^k and Y_q^k are shown in Equation 1.28.

$$\begin{aligned} B_0^k &= \int_0^\infty R_{nl}^2(r) r^k dr \sqrt{\frac{4\pi}{2k+1}} Y_0^k \sum_L \frac{Z_L e^2}{R_L^{k+1}} \\ B_q^k &= \int_0^\infty R_{nl}^2(r) r^k dr \sqrt{\frac{4\pi}{2k+1}} Re\ Y_q^k \sum_L \frac{Z_L e^2}{R_L^{k+1}} \\ B_q'^k &= \int_0^\infty R_{nl}^2(r) r^k dr \sqrt{\frac{4\pi}{2k+1}} Im\ Y_q^k \sum_L \frac{Z_L e^2}{R_L^{k+1}} \end{aligned} \tag{1.28}$$

L are the ligands responsible for the crystal field at a distance R_L, Z their charge and e the elementary charge. Often, instead of B_q^k, the equivalent structural parameters A_k^q are utilised as shown below.

$$B_q^k = a \times A_k^q \langle r^k \rangle \tag{1.29}$$

Table 1.5 *Expectation values $\langle r^k \rangle$ in a.u. [38]*

	$\langle r^1 \rangle$	$\langle r^2 \rangle$	$\langle r^3 \rangle$	$\langle r^4 \rangle$	$\langle r^5 \rangle$	$\langle r^6 \rangle$
Ce^{3+}	0.97	1.17	1.73	3.08	6.44	15.55
Pr^{3+}	0.93	1.08	1.55	2.65	5.36	12.53
Nd^{3+}	0.90	1.01	1.39	2.31	4.53	10.31
Sm^{3+}	0.84	0.89	1.15	1.81	3.38	7.32
Eu^{3+}	0.82	0.84	1.06	1.62	2.96	6.28
Gd^{3+}	0.79	0.79	0.98	1.46	2.61	5.45
Tb^{3+}	0.77	0.75	0.91	1.33	2.33	4.76
Dy^{3+}	0.75	0.71	0.84	1.21	2.08	4.19
Ho^{3+}	0.74	0.68	0.79	1.11	1.87	3.71
Er^{3+}	0.72	0.65	0.74	1.02	1.69	3.31
Tm^{3+}	0.70	0.62	0.69	0.94	1.54	2.97
Yb^{3+}	0.69	0.60	0.65	0.87	1.40	2.67

a is a constant for each B_q^k and A_k^q pair [29], and $\langle r^k \rangle$ represents the average or expectation value of r^k, where r is the nucleus–electron distance of the lanthanide ion, given by

$$\langle r^k \rangle = \int_0^\infty R_{nl}^2(r) r^k dr \tag{1.30}$$

Tabulated values of $\langle r^k \rangle$ for all Ln^{3+} are summarised in Table 1.5.

$(C_q^k)_i$ are the related tensor operators, which transform as the spherical harmonics and are given by

$$(C_q^k)_i = \sqrt{\frac{4\pi}{2k+1}} Y_q^k(i) \tag{1.31}$$

1.3.4 The Crystal Field Parameters B_q^k and Symmetry

The integer k runs in the range 0–7 and the parameters containing even values of k are responsible for the crystal field splitting, while those with odd values influence the intensity of the induced electronic dipole transitions (see Section 1.3.10 for more details) [8,9]. q is also an integer and its values depend on the symmetry of the crystal field and the magnitude of k, since $|q| \leq k$. The possible combinations of k and q for the crystal field parameters are given in Table 1.6 and the symmetry elements contained in the crystal field parameters are summarised in Table 1.7.

The B_0^0 coefficient is notably absent from these tables; since it is spherically symmetric, it acts equally on all f^N configurations. In energy level calculations it can therefore be incorporated into all spherically symmetric interactions and does not need to be considered individually.

Table 1.6 *Values of* q *allowed as a function of the symmetry elements of the crystal field [30]*

Symmetry element present	Values of q allowed
C_n (coincident with main axis)	$\|q\| \leq k$, but is integer of n
σ_h (xy-plane)	Odd $k \Rightarrow q$ odd or $q \neq$ zero
	Even $k \Rightarrow q$ even
σ_v (xz-plane)	No imaginary terms
i (inversion center)	k even
C_2'	Odd $k \Rightarrow q \neq$ zero
	Odd $k + \|q\| \Rightarrow$ no real terms
	Even $k + \|q\| \Rightarrow$ no imaginary terms
S_n (coincident with main axis)	Odd $k \Rightarrow q \neq$ zero
	Odd $k + \|q\| \Rightarrow q \neq n$-fold
	Even $k + \|q\| \Rightarrow q \neq (2x+1)n/2$ ($x = 0, 1, 2, \ldots$)

Table 1.7 *Symmetry elements of the crystal field parameters B_q^k [30]*

q	0	1	2	3	4	5	6	7
B_q^1	C_∞, σ_v	σ_h, σ_v						
B_q^2	C_∞, i, $C2\prime$, S_4, σ_h	σ_v, i, $C2\prime$	C_2, i, C_2', σ_h, σ_v					
B_q^3	C_∞, σ_v	σ_h, σ_v	C_2, σ_v, S_4	C_3, σ_h, σ_v				
B_q^4	C_∞, i, C_2', S_4, σ_h	σ_v, i, C_2'	C_2, i, C_2', σ_h, σ_v	C_3, i, C_2', σ_v, S_6	C_4, i, C_2', σ_h, σ_v, S_4			
B_q^5	C_∞, σ_v	σ_h, σ_v	C_2, σ_v, S_4	C_3, σ_h, σ_v	C_4, σ_v	C_5, σ_h, σ_v		
B_q^6	C_∞, i, C_2', S_4, σ_h	σ_v, i, C_2'	C_2, i, C_2', σ_h, σ_v	C_3, i, C_2', σ_v, S_6	C_4, i, C_2', σ_h, σ_v, S_4	C_5, i, C_2', σ_v	C_6, i, C_2', σ_h, σ_v, S_6	
B_q^7	C_∞, σ_v	σ_h, σ_v	C_2, σ_v, S_4	C_3, σ_h, σ_v	C_4, σ_v	C_5, σ_h, σ_v	C_6, σ_v	C_7, σ_h, σ_v
$B_q'^1$		σ_h, σ_d, C_2'						
$B_q'^2$		σ_d, i	C_2, i, σ_h, σ_d					
$B_q'^3$		σ_h, σ_d, C_2'	C_2, C_2', σ_d, S_4	C_3, C_2', σ_h, σ_d				
$B_q'^4$		σ_d, i	C_2, i, σ_h, σ_d	C_3, i, σ_d, S_6	C_4, i, σ_h, σ_d, S_4			
$B_q'^5$		σ_h, σ_d, C_2'	C_2, C_2', σ_d, S_4	C_3, C_2', σ_h, σ_d	C_4, C_2', σ_d	C_5, C_2', σ_h, σ_d		
$B_q'^6$		σ_d, i	C_2, i, σ_h, σ_d	C_3, i, σ_d, S_6	C_4, i, σ_h, σ_d, S_4	C_5, i, σ_d	C_6, i, σ_h, σ_d, S_6	
$B_q'^7$		σ_h, σ_d, C_2'	C_2, C_2', σ_d, S_4	C_3, C_2', σ_h, σ_d	C_4, C_2', σ_d	C_5, C_2', σ_h, σ_d	C_6, C_2'	C_7, C_2', σ_h, σ_d

The expression for H_{cf} varies depending on the symmetry of the crystal field, as shown by the information in Tables 1.3 and 1.4. For example, if the metal ion is in a site of C_{2v} symmetry, which includes two mirror planes and one C_2 axis, the expression for H_{cf} becomes:

$$H_{cf} = \sum_{k=2,4,6} B_0^k C_0^k + \sum_{k=2,4,6} B_2^k \left(C_2^k + C_{-2}^k\right) + \sum_{k=4,6} B_4^k \left(C_4^k + C_{-4}^k\right) + B_6^6 \left(C_6^6 + C_{-6}^6\right) \quad (1.32)$$

Complete expressions for the summations for symmetry point groups of interest in coordination chemistry can be found for example in Reference [30].

Further discussion of the crystal field perturbation and crystal field parameters will be continued in Section 1.3.7.

As stated, the crystal field lifts the degeneracy of the J levels. However, in the case of Kramers' ions, which have an odd number of electrons and for which therefore J is half-integer, the degeneracy is not completely removed and each sub-level is two-fold degenerate and therefore a Kramers' doublet [39]. Nonetheless, the lifting of the degeneracy is related to the symmetry around the metal ion, and the number of new M_J sub-levels as a function of symmetry is summarised in Table 1.8.

In the case of the Eu(III) ion, where ground and excited state manifolds are well-separated, this direct dependence of the number of M_J levels on the crystal field symmetry is often utilised to determine the point group symmetry of the metal ion in a complex or solid state material from the emission spectra. This method of descending symmetry is performed with the help of a diagram such as the one shown in Fig. 1.5 [41]. A similar analysis can also be performed on the basis of absorption spectra.

By using the reasoning above, the splitting of the $4f^6$ configuration of Eu^{3+} in O_h symmetry will be as shown in Fig. 1.6.

Table 1.8 *Number of new* M_J *sub-levels for a parent J term split by the crystal field in a given group symmetry [13,40]*

Symmetry	Integer *J*						
	0	1	2	3	4	5	6
Icosahedral Ih	1	1	1	2	2	3	4
Cubic O_h, O, T_d, T_h, T	1	1	2	3	4	4	6
Hexagonal D_{6h}, D_6, C_{6v}, C_{6h}, D_{3h}, C_{3h}, D_{3d}, D_3, C_{3v}, S_6, C_3	1	2	3	5	6	7	9
Pentagonal D_{5h}, C_{5h}, C_{5v}, C_5, D_5	1	2	3	4	5	7	8
Tetragonal D_{4h}, D_4, C_{4v}, C_{4h}, C_4, D_{2d}, S_4	1	2	4	5	7	8	10
Low D_{2h}, D_2, C_{2v}, C_{2h}, C_2, C_s, S_2, C_1	1	3	5	7	9	11	13

	Half-integer *J*								
	1/2	3/2	5/2	7/2	9/2	11/2	13/2	15/2	17/2
Cubic	1	1	2	3	3	4	5	6	6
Other symmetries	1	2	3	4	5	6	7	8	9

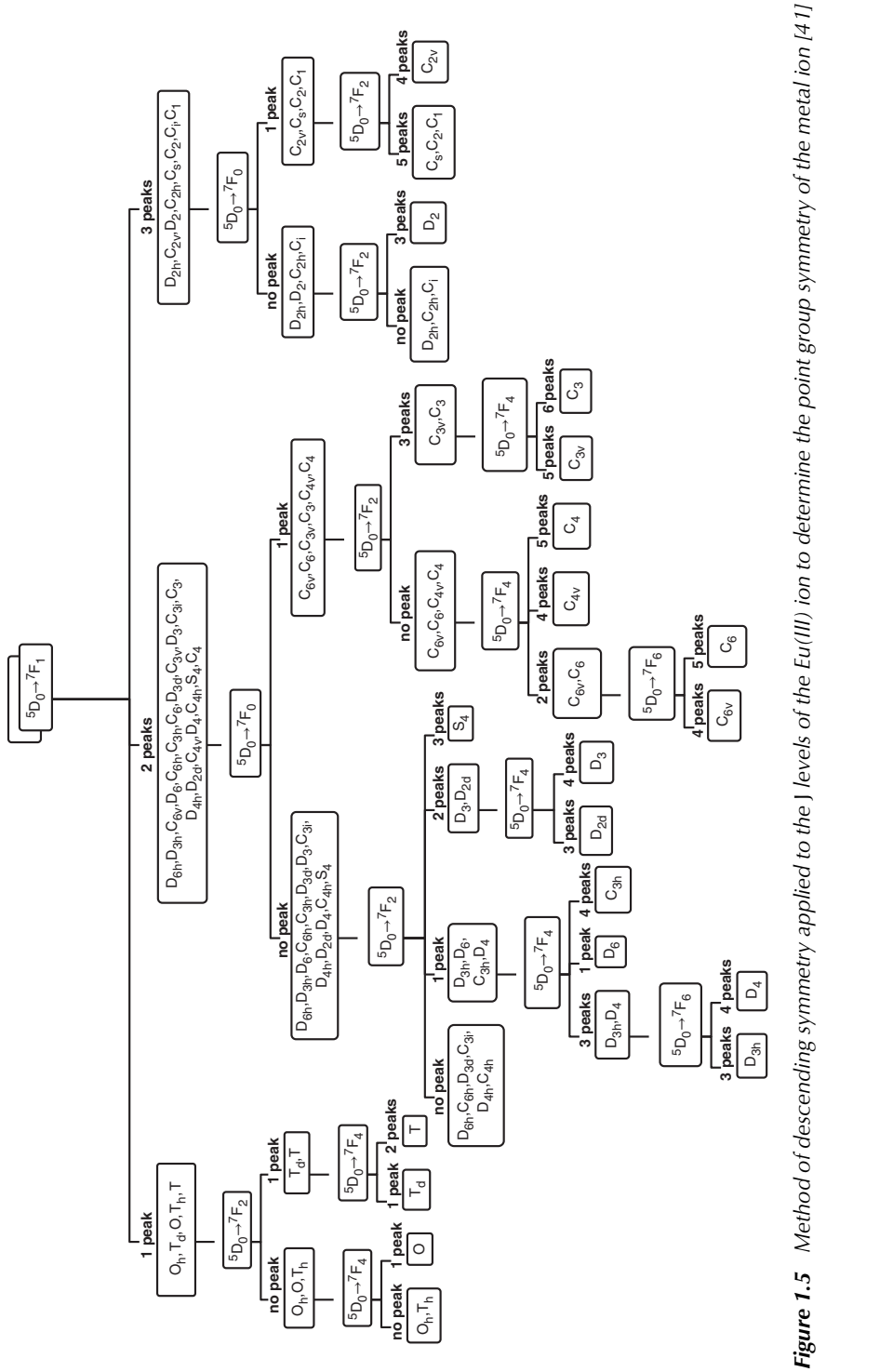

Figure 1.5 *Method of descending symmetry applied to the J levels of the Eu(III) ion to determine the point group symmetry of the metal ion [41]*

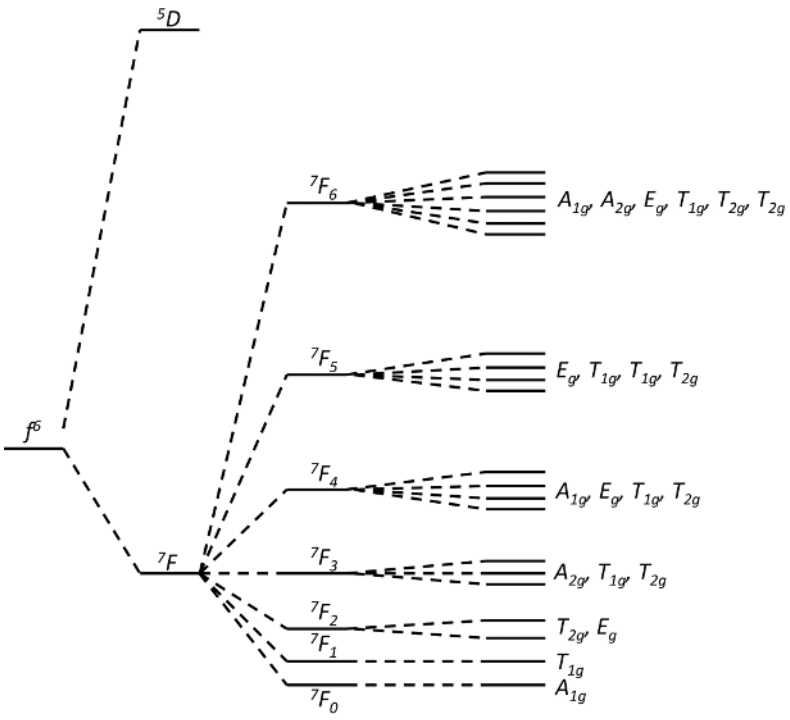

Figure 1.6 *Stark levels (energies not to scale) with corresponding symmetry labels for* Eu^{3+} *in* O_h *symmetry*

The symmetries of the individual Stark levels indicated in Fig. 1.6 can be determined as shown in Section 1.3.9 and a complete list of the Stark level symmetries for all point groups can be found in Reference [30].

1.3.5 Energies of Crystal Field Split Terms

Estimation of the crystal field energy levels occurs through diagonalisation of the Hamiltonian matrix in Equation 1.33.

$$\left\langle \psi_{f^n SLJM_J} \middle| H_{cf} \middle| \psi_{f^n S'L'J'M_{J'}} \right\rangle \tag{1.33}$$

After substituting Equation 1.26 into Equation 1.33, it can be shown that the matrix elements are described by Equation 1.34 [29,42].

$$\sum_{k,q} B_q^k \left\langle \psi_{f^n SLJM_J} \middle| \sum_i (C_q^k)_i \middle| \psi_{f^n SLJM_{J'}} \right\rangle = (-1)^{2J-M_J+S+L+k+3} 7(2J+1) \times \begin{pmatrix} 3 & k & 3 \\ 0 & 0 & 0 \end{pmatrix} \begin{pmatrix} J & k & J \\ -M_J & q & M_{J'} \end{pmatrix} \begin{Bmatrix} J & J & k \\ L & L & S \end{Bmatrix} \left\langle \psi_{f^n SL} \middle\| U^k \middle\| \psi_{f^n SL} \right\rangle \tag{1.34}$$

The terms in parentheses are 3-*j* symbols and the term in braces is a 6-*j* symbol. The first 3-*j* symbol indicates the coupling of the angular momenta $l = 3$ between final and initial states, the second 3-*j* and the 6-*j* symbol denote the coupling of two, J and M_J, and three, J, L and S, angular momenta, respectively. These symbols are tabulated in [35] or can be calculated in *Mathematica* [43] or by using several calculators available online. While the general formulas for the symbols are complicated, it can be shown that for the first 3-*j* symbol to be non-zero the following relationship must hold:

$$\left|3 - 3\right| \leq k \leq 3 + 3 \text{ or } k = 0 - 6.$$

The second 3-*j* symbol will be non-zero for: $-M_J + q + M_J{}' = 0 \Leftrightarrow M_J - M_J{}' = q$ and $\left|J - J\right| \leq k \leq J + J$ or $k \leq 2J$ and $\left|q\right| \leq k$.

These conditions for the 3-*j* symbols dictate the selection of $k = 0, 2, 4, 6$ for the crystal field splitting.

The 6-*j* symbol will be non-zero for $|J - k| \leq J' \leq J + k$ and $|L' - S| \leq L \leq L' + S$.

The doubly reduced matrix elements $\langle \psi_{l^n SL} \parallel U^k \parallel \psi_{l^n S'L'} \rangle$ are specific to a given lanthanide ion. It was shown that the crystal field does not affect them substantially. Therefore, instead of calculating them for each system, the values tabulated by Nielson and Koster can be used [34].

With all of these tabulated values, only the B_q^k needs to be determined to evaluate the energy level splitting based on the crystal field and its symmetry.

For Pr^{3+}, which has the valence configuration f^2, in D_{3h} symmetry the reduced matrix elements $\langle U^4 \rangle$ and $\langle U^6 \rangle$ vanish (Table 1.9) and only $\langle U^2 \rangle$ needs to be evaluated. Therefore, for the $^3P_2$ term, with $L = S = 0, J = 2, q = 0, k = 2$ (see above for the discussion of the values of q and k depending on symmetry), and $M_J = 0, \pm 1, \pm 2$, it can be shown with Equation 1.34 above that

$$\langle f^2\, {}^3P_2\, 20 | H_{cf} | f^2\, {}^3P_2\, 20 \rangle = -\frac{1}{5} B_0^2$$

$$\langle f^2\, {}^3P_2\, 21 | H_{cf} | f^2\, {}^3P_2\, 21 \rangle = -\frac{1}{10} B_0^2$$

$$\langle f^2\, {}^3P_2\, 22 | H_{cf} | f^2\, {}^3P_2\, 22 \rangle = \frac{1}{5} B_0^2$$

$$\langle f^2\, {}^3P_2\, 20 | H_{cf} | f^2\, {}^3P_2\, 00 \rangle = \frac{\sqrt{2}}{5} B_0^2$$

$$\langle f^2\, {}^3P_2\, 21 | H_{cf} | f^2\, {}^3P_2\, 11 \rangle = \frac{3}{10} B_0^2$$

etc.

Similar reasoning for the $^3P_0$ and $^3P_1$ terms allows the drawing of the diagram shown in Fig. 1.7, which represents the relative energies of the crystal field split terms.

1.3.6 Zeeman Effect

As mentioned above, in the case of Kramers' ions with non-integer value of J, the crystal field does not completely lift the degeneracy of the J levels. This degeneracy can however

Table 1.9 *Selected doubly reduced matrix elements* $\langle \psi_{f^n SL} \| U^k \| \psi_{f^n S'L'} \rangle$ *for the* f^2 Pr^{3+} *ion [34]*

Pr^{3+}, f^2	$\langle \psi_{f^n SL} \| U^2 \| \psi_{f^n S'L'} \rangle$	$\langle \psi_{f^n SL} \| U^4 \| \psi_{f^n S'L'} \rangle$	$\langle \psi_{f^n SL} \| U^6 \| \psi_{f^n S'L'} \rangle$
$^3P/^3P$	$-3/\sqrt{14}$	0	0
$^3P/^3F$	$\sqrt{6/7}$	$-\sqrt{11/21}$	0
$^3F/^3F$	$-1/3$	$-1/3$	$-1/3$
$^3F/^3H$	$2/3\sqrt{11/7}$	$\sqrt{65/63}$	$-1/3\sqrt{14}$

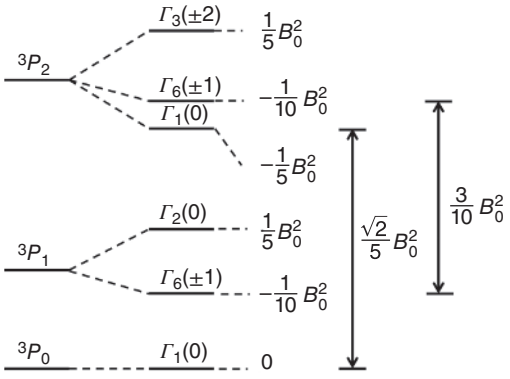

Figure 1.7 *Relative energies (not to scale) of the crystal field split* ^3P_J *(J = 0, 1, 2) terms of* Pr^{3+} *in* D_{3h} *symmetry*

be lifted in the presence of an external magnetic field and is often referred to as the Zeeman effect [44]. The magnitude of the splitting is proportional to the strength of the applied magnetic field. The expression for the Hamiltonian H_z is given in Equation 1.35 [42].

$$H_z = g\,\mu_B B \cdot J \tag{1.35}$$

μ_B is the Bohr Magneton; B is the magnitude of the external magnetic field and g is Landé's factor (Equation 1.36) in the *LS* coupling scheme.

$$g = 1 + \frac{J(J+1) - L(L+1) + S(S+1)}{2J(J+1)} \tag{1.36}$$

The effective magnetic moment μ is given by Equation 1.37.

$$\mu = -\mu_B g J \tag{1.37}$$

If the applied magnetic field is parallel to the z-axis of a crystal, the splitting energy E_Z is given by

$$E_Z = \mu_B g B \langle JM_z | J_z | JM_z \rangle \tag{1.38}$$

M_Z is the quantum number associated with this perturbation. If, on the other hand, the Zeeman interaction is anisotropic, the Hamiltonian in Equation 1.35 should be re-written as

$$H_Z = \mu_B (g_x B_x J_x + g_y B_y J_y + g_z B_z J_z) \tag{1.39}$$

with the components along the x, y and z axes designated by the appropriate subscripts.

1.3.7 Point Charge Electrostatic Model

Qualitative estimation of the B_q^k parameters and therefore of the symmetry around the metal ion and the positions of the energy levels can be done utilising the point charge electrostatic model (PCEM), which assumes that the electric field acting on the central metal ion is generated by the ligands as negative point charges, and all ligands have the same charge. These point charges are arranged according to the correct symmetry of the metal ion site. Taking into account Equations 1.27 and 1.30, and considering that N ligands will be at a distance R_A and M ligands at a distance R_B ($R_A < R_B$), Equation 1.28 can be re-written as Equation 1.40.

$$\begin{aligned}
B_0^k &= \textstyle\sum_{A=1}^{N} Z_L e^2 \frac{\langle r^k \rangle}{R_A^{k+1}} \sqrt{\frac{4\pi}{2k+1}} Y_0^k(\theta_A, \phi_A) + \sum_{B=1}^{M} Z_L e^2 \frac{\langle r^k \rangle}{R_B^{k+1}} \sqrt{\frac{4\pi}{2k+1}} Y_0^k(\theta_B, \phi_B) \\
B_q^k &= \textstyle\sum_{A=1}^{N} Z_L e^2 \frac{\langle r^k \rangle}{R_A^{k+1}} \sqrt{\frac{4\pi}{2k+1}} (-1)^q \mathrm{Re}\ Y_q^k(\theta_A, \phi_A) \\
&\quad + \textstyle\sum_{B=1}^{M} Z_L e^2 \frac{\langle r^k \rangle}{R_B^{k+1}} \sqrt{\frac{4\pi}{2k+1}} (-1)^q \mathrm{Re}\ Y_q^k(\theta_B, \phi_B) \\
B_q'^k &= \textstyle\sum_{A=1}^{N} Z_L e^2 \frac{\langle r^k \rangle}{R_A^{k+1}} \sqrt{\frac{4\pi}{2k+1}} (-1)^q \mathrm{Im} Y_q^k(\theta_A, \phi_A) \\
&\quad + \textstyle\sum_{B=1}^{M} Z_L e^2 \frac{\langle r^k \rangle}{R_B^{k+1}} \sqrt{\frac{4\pi}{2k+1}} (-1)^q \mathrm{Im} Y_q^k(\theta_B, \phi_B)
\end{aligned} \tag{1.40}$$

θ_L and ϕ_L are coordinates of the ligand point charges. Since the positions of the ligands are important to indicate the angles, and therefore the sign of the crystal field parameters, the choice of molecular axes should follow the usual convention, in which the axis of highest rotational symmetry coincides with the z-axis. Also, with judicial choice of the molecular axes, it is possible in some cases to set $B_q'^k = 0$ [30]. Finally, since the radial parts of the parameters B_0^k and B_q^k are the same, the ratio B_q^k / B_0^k does not have a radial component and will be a constant for a given symmetry. Therefore, only the B_0^k with $k = 2$, 4 and 6 needs to be fit.

For example, if the metal is situated in a hypothetical D_{3h} symmetry environment with three equidistant ligands, the parameters of interest are given by the expression for H_{cf}

below, as demonstrated in Section 1.3.4:

$$H_{cf} = B_0^2 C_0^2 + B_0^4 C_0^4 + B_0^6 C_0^6 + B_6^6 (C_{-6}^6 + C_6^6)$$

Since the ligands span a triangle and their position angles θ/ϕ are equal to 90°/90°, 90°/120° and 90°/330°, with the help of the tabulated spherical harmonics, and substituting in Equation 1.40, it follows that:

$$B_0^2 = -\frac{3}{2} Ze^2 \frac{\langle r^2 \rangle}{R^3}$$

$$B_0^4 = \frac{9}{8} Ze^2 \frac{\langle r^4 \rangle}{R^5}$$

$$B_0^6 = -\frac{15}{16} Ze^2 \frac{\langle r^6 \rangle}{R^7}$$

$$B_6^6 = -\frac{3\sqrt{231}}{32} Ze^2 \frac{\langle r^6 \rangle}{R^7}$$

By utilising a similar procedure, it can be shown that for a general prismatic polyhedron with p axial ligands, n equatorial ligands and m ligands in the base of the prism [30]

$$\begin{aligned} B_0^2 &= Ze^2 \frac{\langle r^2 \rangle}{R^3} \left[p - \frac{n}{2} + m(3\cos^2\theta - 1) \right] \\ B_0^4 &= Ze^2 \frac{\langle r^4 \rangle}{R^5} \left[p + \frac{3n}{8} + \frac{m}{4}(35\cos^4\theta - 30\cos^2\theta + 3) \right] \\ B_0^6 &= Ze^2 \frac{\langle r^2 \rangle}{R^7} \left[p - \frac{5n}{16} + \frac{m}{8}(231\cos^6\theta - 315\cos^4\theta + 105\cos^2\theta - 5) \right] \end{aligned} \tag{1.41}$$

Some polyhedra are relatively common for lanthanide ion complexes, and they will be discussed here in more detail. They are the square antiprism, the tricapped trigonal prism and the monocapped square antiprism, shown below in Fig. 1.8. The metal ion is situated in the centre of the polyhedron and the ligands, as point charges, are located at the vertices. The proper axis of highest symmetry is chosen to coincide with the z-axis, as mentioned before.

The previous section described the expressions for the crystal field parameters for regular polyhedra. However, most frequently the geometry around the lanthanide ion departs more or less drastically from the regular geometry. Of the crystal field parameters, B_0^k depends on θ, while B_q^k depends both on θ and ϕ. Therefore, distortions of both angles will affect both sets of parameters, while changes in ϕ will affect only the latter. When fitting the parameters, it is common to do an initial fit at a higher symmetry and then refine at the lower, coordination compound-appropriate symmetry.

The locations of the point charges are given in Table 1.10 and different coordination polyhedra and their parameters are described below.

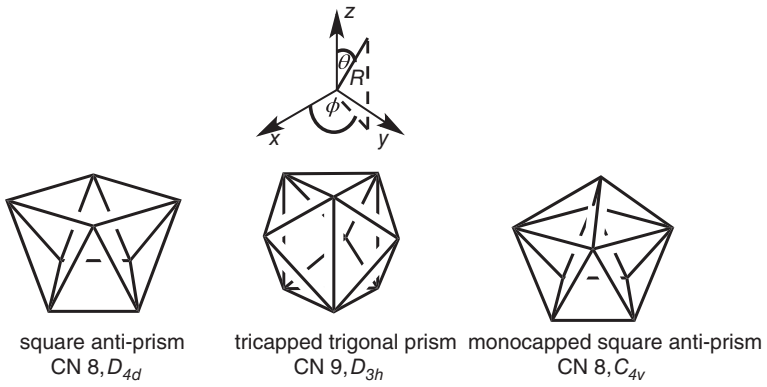

Figure 1.8 *Common coordinat ion polyhedra for lanthanide ions, shown with the Cartesian and polar coordinate system*

1.3.7.1 Square Antiprism

This coordination geometry is often encountered when the metal ion has the coordination number (CN) 8, for which $p = n = 0$ and $m = 4$. The point group symmetry is D_{4d}, with four ligands spanning a square above and four ligands the other square below the central ion. An S_8 improper axis of rotation coincides with the z-axis and passes through the metal ion and in between all eight ligand point charges. The square antiprism is obtained by 22.5° clockwise and counter-clockwise of the top and bottom faces with respect to the metal ion from a cube. The square antiprism will be elongated when $\theta > 54.74°$ and compressed when $\theta < 54.74°$. The angle φ can distort from $2 \times 22.5°$ by φ, upon which the symmetry will decrease to D_4. Substituting into Equation 1.40 yields the following B_q^k parameters for a distorted square antiprism.

Table 1.10 *Angular coordinates of the ligands as point charges for the three coordination polyhedra and distorted coordination polyhedra*[a]

θ/φ [°]	$D_{4d} \rightarrow D_4$	$D_{3h} \rightarrow D_3$	$C_{4v} \rightarrow C_4$
Atoms spanning top face	$\theta/45 + \varphi$	$\theta/90 + \varphi$	$125.7/45 + \varphi$
	$\theta/135 + \varphi$	$\theta/210 + \varphi$	$125.7/135 + \varphi$
	$\theta/225 + \varphi$	$\theta/330 + \varphi$	$125.7/225 + \varphi$
	$\theta/315 + \varphi$		$125.7/315 + \varphi$
Atoms spanning bottom face	$180 - \theta/45 - \varphi$	$180 - \theta/90 - \varphi$	$70.1/45 - \varphi$
	$180 - \theta/135 - \varphi$	$180 - \theta/210 - \varphi$	$70.1/135 - \varphi$
	$180 - \theta/225 - \varphi$	$180 - \theta/330 - \varphi$	$70.1/225 - \varphi$
	$180 - \theta/315 - \varphi$		$70.1/315 - \varphi$
Capping atoms	—	90/30	0/0
		90/150	
		90/270	

[a] φ is the angle by which the bottom and top faces distort from the regular polyhedron, past the 45° angle in the case of the square antiprism and monocapped square antiprism and 0° angle in the case of the tricapped trigonal prism.

$$B_0^2 = Ze^2 \frac{\langle r^2 \rangle}{R^3} 4(3\cos^2\theta - 1)$$

$$B_0^4 = Ze^2 \frac{\langle r^4 \rangle}{R^5} (35\cos^4\theta - 30\cos^2\theta + 3)$$

$$B_4^4 = -\frac{\sqrt{70}}{2} Ze^2 \frac{\langle r^4 \rangle}{R^5} \sin^4\theta \cos 4\varphi$$

$$B_0^6 = \frac{1}{2} Ze^2 \frac{\langle r^6 \rangle}{R^7} (231\cos^6\theta - 315\cos^4\theta + 1 - 5\cos^2\theta - 5)$$

$$B_4^6 = \frac{21}{2\sqrt{14}} Ze^2 \frac{\langle r^6 \rangle}{R^7} \sin^4\theta (11\cos^2\theta - 1)\cos 4\varphi$$

As can be seen from the equations above, parameters B_4^4 and B_4^6 have the distortion angle φ in their expression and are therefore indicators of the magnitude of the distortion of the square antiprism. Along similar lines, $(3\cos^2\theta - 1)$ vanishes for 54.74°, the cubic angle, and therefore the presence of the parameter B_0^2 is an indication of the distortion of the square antiprism from the higher symmetry cube.

1.3.7.2 Tricapped Trigonal Prism

The tricapped trigonal prism is a commonly encountered coordination polyhedron for CN 9, although often distorted. For this polyhedron $p = 0$ and $n = m = 3$. The symmetry is D_{3h} and the polyhedron has three atoms at the top spanning a triangular face and three atoms at the bottom spanning another triangular face, eclipsed with the top face. A C_3 axis contains the metal ion and is collinear with the z-axis. The point charges spanning the top and bottom faces will be at a distance R_A, while the capping charges will be at a distance R_B. When the top and base faces twist by $2 \times \varphi$, the symmetry decreases to D_3.

$$B_0^2 = Ze^2 \frac{\langle r^2 \rangle}{R^3} \frac{9}{2} (2\cos^2\theta - 1)$$

$$B_0^4 = Ze^2 \frac{\langle r^4 \rangle}{R^5} \frac{3}{8} (70\cos^4\theta - 60\cos^2\theta + 9)$$

$$B_3^4 = Ze^2 \frac{\langle r^4 \rangle}{R^5} \frac{3\sqrt{35}}{2} (\sin^3\theta \cos\theta \sin 3\varphi)$$

$$B_0^6 = Ze^2 \frac{\langle r^6 \rangle}{R^7} \frac{3}{16} (462\cos^6\theta - 630\cos^4\theta + 210\cos^2\theta - 15)$$

$$B_3^6 = Ze^2 \frac{\langle r^6 \rangle}{R^7} \frac{3\sqrt{105}}{8} \sin^3\theta (11\cos^3\theta - 3\cos\ \theta)\sin 3\varphi$$

$$B_3^6 = Ze^2 \frac{\langle r^6 \rangle}{R^7} \frac{3\sqrt{231}}{32} (2\sin^6\theta \cos 6\varphi + 1)$$

1.3.7.3 Monocapped Square Antiprism

This coordination polyhedron is a special case of the square antiprism, with $p = 1$, $n = 0$ and $m = 4$, as a capping atom is added on top of the top face of the antiprism, which results in a top face with a larger area. The symmetry around the metal ion is C_{4v} with CN 9, with a C_4 axis passing through the metal ion and the capping point charge.

$$B_0^2 = Ze^2 \frac{\langle r^2 \rangle}{R^3} \left[12\cos^2\theta - 11\right]$$

$$B_0^4 = Ze^2 \frac{\langle r^4 \rangle}{R^5} \left[35\cos^4\theta - 30\cos^2\theta + 4\right]$$

$$B_0^6 = Ze^2 \frac{\langle r^6 \rangle}{R^7} \left[-\frac{1}{2} + \frac{1}{2}(231\cos^6\theta - 315\cos^4\theta + 105\cos^2\theta)\right]$$

The crystal field parameters B_4^4 and B_4^6, which account for the distortions from C_{4v} symmetry, are analogous to the square antiprismatic case.

1.3.8 Other Methods to Estimate Crystal Field Parameters

The point-charge electrostatic model is useful in illustrating how symmetry influences the signs of the crystal field parameters B_q^k. However, it does not usually result in accurate determinations of their magnitude and therefore other methods have been developed that lead to a better estimation. One such approach is based on the angular overlap model AOM developed and expanded to the *f* elements by Jørgensen [45]. Another approach is the simple overlap model SOM, proposed by Malta [46].

1.3.8.1 Angular Overlap Model

The angular overlap model (AOM) considers the existence of weak covalent interactions between the Ln(III) orbitals and the ligand orbitals which perturb the metal-based orbitals. The perturbation is proportional to the overlap of the metal and ligand orbitals and is evaluated in terms of the anti-bonding energy E^* of the *f* orbital considered, as the anti-bonding orbital is mostly metal in character. For a complex with N ligands L, ML_N, this energy is described by Equation 1.42 [47].

$$E^* = e_\lambda \sum_{j=1}^{N} (F_\lambda^l)^2 \tag{1.42}$$

e_λ are quantities that depend on the radial functions of the metal M and the ligands and on the bond distances between the two and the nature of the interaction [$\lambda = 0$ (σ), 1 (π)], l is the angular momentum quantum number, and F_λ^l are the angular overlap integrals. For an ML_9 system with D_{3h} symmetry, for which was shown above that $H_{cf} = B_0^2C_0^2 + B_0^4C_0^4 + B_0^6C_0^6 + B_6^6(C_{-6}^6 + C_6^6)$, the energies of the *f* orbitals in units of e_λ are shown in Table 1.11. The energies for other symmetries can be found in Reference [47].

Table 1.11 *Energies of the* f *orbitals in an ML_9 complex in units of* e_λ *for* D_{3h} *symmetry [47]*

f Orbital	Symmetry	e_σ	e_π
z^3	a_2''	3/16	117/32
xz^2	e'	117/64	213/128
yz^2			
$z(x^2-y^2)$	e''	45/32	195/64
xyz			
$x(x^2-3y^2)$	a_1'	75/32	45/64
$y(3x^2-y^2)$	a_2'	0	135/32

Based on these energies, the splitting pattern shown in Fig. 1.9 for the *f* orbitals of complex ML_9 in D_{3h} symmetry can be deduced.

The $B_q^k C_q^k$ parameters can be expressed in terms of the AOM e_λ [48], and for the $B_0^2 C_0^2$ in D_{3h} symmetry [49].

$$B_0^2 C_0^2 = \frac{3}{7}\sqrt{5\pi}\left[\frac{(2f_1+3)}{2f_1}\right] \times (-1 + 4f_2 - 6f_2 \sin^2\theta) e_{\sigma_1}$$

with $f_1 = \frac{e_{\sigma_1}}{e_{\pi_1}} = \frac{e_{\sigma_2}}{e_{\pi_2}} = \frac{e_\sigma}{e_\pi}$ and $f_2 = \frac{e_{\sigma_2}}{e_{\sigma_1}} = \frac{e_{\pi_2}}{e_{\pi_1}}$, for the ligands at distances R_1 and R_2.

Using these considerations, for Pr(III) in $LaCl_3$, Urland calculated $B_0^2 C_0^2 = 164\,\text{cm}^{-1}$, which compares well with the experimental value of $150\,\text{cm}^{-1}$ [49].

1.3.8.2 Simple Overlap Model

In the simple overlap model (SOM), the crystal field experienced by the 4*f* electrons is generated by point charges located in small regions around the middle distance between the lanthanide ion and its ligands. These regions of charge are not necessarily positioned exactly in between the lanthanide ion and the ligands; therefore, a correction factor, β_L, which is given by Equation 1.43, is introduced to account for this asymmetry.

$$\beta_L = \frac{1}{1 \pm \rho_L} \tag{1.43}$$

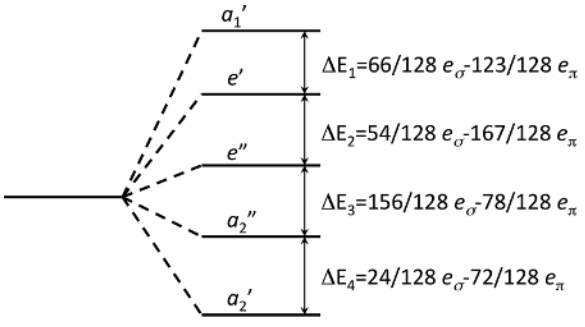

Figure 1.9 *Splitting pattern based on the AOM of the* f *orbitals of complex ML_9 in* D_{3h} *symmetry*

In this equation, ρ_L is an additional correction factor to the position of the region of charge. A positive sign indicates that this region is shifted towards the ligand, which is usually observed for small electronegative species such as O and F. The negative sign will be used when the ligand is bulkier and contains atoms such as N and Cl and the region of charge is displaced towards the lanthanide ion. In initial publications on $LaCl_3$:Nd^{3+} ρ_L was set at 0.05 and therefore $\beta_L = 1.1$ with the region of charge towards the lanthanide [46], and on YOCl:Eu^{3+} $\beta_O = 0.95$ and $\beta_{Cl} = 1.05$, showing the centroid shifted towards O for the Ln–O interaction and towards Ln for the Ln–Cl interaction, respectively [50]. It was later suggested that ρ_L can be estimated using Equation 1.44 [51].

$$\rho_L = 0.05\left(\frac{R_0}{R_L}\right)^{3.5} \tag{1.44}$$

R_0 corresponds the shortest M−L bond and R_L is the M−L bond distance for the ligand L of interest.

The charge of the region between the ligand and the lanthanide is equal to $-g_L e\rho$, where ρ is proportional to the magnitude of orbital overlap between lanthanide and ligand, e is the electron charge and g_L is the ligand charge factor. Instead of the ligand charge Z_L, which is used in the PCEM, in the SOM g_L is used in the estimation of B_q^k (Equation 1.40). Both crystal field parameters are related by Equation 1.45.

$$B_q^k(\text{SOM}) = \rho(2\beta)^{k+1} B_q^k(\text{PCEM}) \tag{1.45}$$

The success of the SOM for estimation of the crystal field parameters can be seen from the data summarised in Table 1.12, which shows the phenomenological B_q^k compared to the numbers obtained through the PCEM, SOM, and through AOM for an acetylacetonato complex of Nd(III).

1.3.9 Allowed and Forbidden *f-f* Transitions

Optical transitions within the 4*f* shell arise due to interaction of the electric and magnetic components of the electromagnetic radiation with the *f* electrons and are therefore either electric or magnetic dipole transitions (ED or MD), respectively. The electric dipole transition can be considered a linear displacement of charge and its direction is reversed through inversion, meaning it has odd parity. The magnetic dipole transition, on the other

Table 1.12 *Comparison of experimental B_q^k [cm^{-1}] with values calculated with PCEM, AOM and SOM for $Nd(btmsa)_3$ [52]*

B_q^k	Phenomenological	PCEM	AOM	SOM
B_0^2	−2912	−4220	−1834	−2964
B_0^4	+920	+370	+1391	+821
B_0^6	−516	−61	−304	−427
B_6^6	±331	±154	±512	±1083

hand, corresponds to a rotational displacement of charge, which, upon inversion, does not change its sense of rotation and therefore has even parity. Which transitions are allowed and which are forbidden is determined by selection rules.

1.3.9.1 Empirical Parameters Describing Optical Transitions

In absorption spectra the peak maxima is reported either as absorbance A or as molar absorptivity ε, which is independent of sample concentration, and they are related as shown in Equation 1.46.

$$A = \varepsilon c l \tag{1.46}$$

c is the sample concentration and l the path length covered by the light through the sample.

In the case of narrow absorption bands, due to signal-to-noise considerations, it is better to report the area of the peak $\int \varepsilon(\overline{\nu}) d\overline{\nu}$ ($\overline{\nu}$ are wavenumbers in cm^{-1}), which is proportional to the peak intensity. Two other quantities, which can be reported instead of ε, are the transition dipole strength D and the oscillator strength P, to which they are related by the following two equations [53].

$$D = 9 \times 10^{-39} \int \frac{\varepsilon(\overline{\nu})}{\overline{\nu}} d\overline{\nu} \tag{1.47}$$

$$P = 4.32 \times 10^{-9} \int \varepsilon(\overline{\nu}) d\overline{\nu} = 4702 \times 10^{29} \times \overline{\nu}_0 \times D \tag{1.48}$$

$\overline{\nu}_0$ is the wavenumber at absorption maximum.

For transitions forbidden by selection rules, $P \ll 1$ and, in the case of the Ln(III), $P \sim 10^{-6}$ esu^2 cm^2 for MD allowed and ED forbidden transitions, with $\varepsilon_{max} < 10\,cm^{-1}\,M^{-1}$, which is habitually on the order of $1\,cm^{-1}\,M^{-1}$.

Correction factors for the dielectric medium, represented by its refractive index n, and for the degeneracy $2J+1$ of the terms are included, since both influence the transition dipole and oscillator strengths. The corrected expressions are given in Equations 1.49 and 1.50.

$$D_{corr.} = \frac{\chi}{2J+1} D \tag{1.49}$$

$$P_{corr.} = \frac{\chi}{2J+1} P \tag{1.50}$$

χ are the dielectric medium correction factors for ED and MD transitions. For absorption, these are given by Equation 1.51.

$$\begin{aligned} \chi_{ED} &= \frac{(n^2+2)^2}{9n} \\ \chi_{MD} &= n \end{aligned} \tag{1.51}$$

For emission, the equations are:

$$\chi_{ED} = \frac{n^2(n^2+2)^2}{9}$$
$$\chi_{MD} = n^3 \tag{1.52}$$

Since many *f-f* transitions of the Ln(III) have both ED and MD components, the overall experimental dipole strength is given by Equation 1.53.

$$D_{\text{exp}} = \frac{1}{2J+1}(\chi_{MD}D_{MD} + \chi_{ED}D_{ED}) \tag{1.53}$$

1.3.9.2 The Spin Rule

For a transition to be spin allowed, the spins of excited and ground state need to be the same. In the case of several *f-f* transitions of the lanthanide ions, these are accompanied by a change in spin and are therefore strictly forbidden. However, as mentioned previously, due to the spin–orbit coupling the total spin quantum number S is no longer completely valid, and therefore this rule is relaxed [53].

1.3.9.3 The Parity Rule

The parity or Laporte rule states that for an optical transition to be allowed, the parity between final and initial states needs to change [53]. Utilising group theory arguments, it can be concluded that, for the transition to be allowed, the totally symmetric irreducible representation Γ_1 (Bethe's symbol, equivalent to Mulliken's symbols A_1) needs to be contained in the direct product shown in Equation 1.54.

$$\Gamma_i \otimes \Gamma \otimes \Gamma_f \tag{1.54}$$

Γ_i and Γ_f are the symmetry labels of the initial and final states and Γ is the symmetry of the operator of the transition being considered. In the case of an electric dipole transition, in which interaction of the electric part of the electromagnetic radiation induces a linear displacement of electric charge in the ion or atom, the operator O_{ED} transforms as x, y and z. It is given by:

$$O_{ED} = -e\sum_i \vec{r}_i \tag{1.55}$$

Since both the operator and the *f* orbitals have *u* (*ungerade*, odd) symmetry, electric dipole transitions are forbidden by the parity rule (see section below on Judd–Ofelt theory and induced electric dipole transitions). The selection rules for these transitions are summarised in Table 1.13.

The magnetic dipole operator O_{MD} induces a rotational displacement of electric charge in the ion or atom due to interaction with the magnetic component of the electromagnetic

Table 1.13 *Selection rules for* f-f *transitions*

Transition	ΔS	ΔL	ΔJ
ED	0	≤ 6	≤ 6 (2,4 or 6 if J or $J' = 0$)
MD	0	0	0, ± 1

radiation. It transforms as R_x, R_y and R_z. Its expression is:

$$O_{MD} = -\frac{e\hbar}{2mc}\sum_i \vec{l}_i + 2\vec{s}_i \tag{1.56}$$

Since O_{MD} has g (*gerade*, even) symmetry and the f orbitals u, magnetic dipole transitions are allowed in centrosymmetric and noncentrosymmetric point groups. However, the selection rules $\Delta J = 0$, 1 (but not $0 \leftrightarrow 0$) are followed (Table 1.13), and so few magnetic dipole transitions, such as the Eu^{3+} $^5D_0 \rightarrow {}^7F_1$ transition, are known.

Electric quadrupole transitions are also possible; despite the even parity of the electric quadrupole operator, the intensity of these transitions is low, and they are less relevant for the lanthanide ions. They will therefore not be addressed here [29].

1.3.9.4 Symmetries of the Terms

To help decide which transitions between energy levels of lanthanide ions are electric or magnetic dipole allowed, depending on the symmetry in which the lanthanide ion is located, it is useful to determine the symmetries of the terms split by the crystal field. This can be done with the rotation formula (Equation 1.57).

$$\chi(C_n) = \frac{\sin\left(J + \frac{1}{2}\right)\alpha}{\sin\frac{\alpha}{2}} \tag{1.57}$$

In this equation, χ is the character of the symmetry operation C_n, and α the rotation angle. For the identity operation $\chi(E) = 2J + 1$, which corresponds to the degeneracy of the term. For the operations σ and i the characters are $\chi(\sigma) = -\chi(C_2)$ and $\chi(i) = -\chi(E)$, respectively. Using these formulas it is possible to determine the reducible representation Γ associated with each term and, upon reduction into its irreducible components, utilising the reduction formula (Equation 1.58), the symmetries of the individual crystal field split terms.

$$a_i = \frac{1}{h}\sum\nolimits_R g_R \cdot \chi_r^{(R)} \cdot \chi_i^{(R)} \tag{1.58}$$

a_i is the number of times the reducible representation Γ_r is contained in the irreducible representation Γ_i, h is the order of the group, g_R is the number of operations in each class R of symmetry operations and χ is the character of the irreducible Γ_i or reducible representation Γ_r for each class R.

Table 1.14 *Multiplication table showing the selection rules for the O_h point group [30]*

O_h	Γ_1^+	Γ_2^+	Γ_3^+	Γ_4^+	Γ_5^+
Γ_1^+	—	—	—	R_x, R_y, R_z	—
Γ_2^+	—	—	—	—	R_x, R_y, R_z
Γ_3^+	—	—	—	R_x, R_y, R_z	R_x, R_y, R_z
Γ_4^+	R_x, R_y, R_z	—	R_x, R_y, R_z	R_x, R_y, R_z	R_x, R_y, R_z
Γ_5^+	—	R_x, R_y, R_z	R_x, R_y, R_z	R_x, R_y, R_z	R_x, R_y, R_z

If J is a half-integer, character tables for double groups are utilised for the reduction, which contain the additional symmetry element R, defined as rotation by 2π and $\chi(\alpha + 2\pi) = -\chi(\alpha)$ [54]. In addition to the symmetry elements of the common character tables, the additional symmetry elements C_2R (same character as C_2), C_n^{n-1} (same character as C_n) and C_n^{n-m} (same character as C_n^m) are present.

For example, Eu(III) has the electronic configuration $4f^6$ with the ground state multiplet $^7F_0$, $^7F_1$, $^7F_2$, $^7F_3$, $^7F_4$, $^7F_5$ and $^7F_6$, in order of increasing energy. Under octahedral symmetry O (order of the group $h = 24$) and utilising the rotation formula (Equation 1.57) it can be shown that $^7F_3$ transforms as the reducible representation Γ_r shown below.

O	E	$6C_4$	$3C_2$	$8C_3$	$6C_2$
Γ_r	7	−1	−1	1	−1

Using the reduction formula (Equation 1.58), it can further be shown that $\Gamma_r = A_2 + T_1 + T_2$ or $\Gamma_r = \Gamma_2 + \Gamma_4 + \Gamma_5$ using Bethe's notation. If the O_h group symmetry is used instead, $\Gamma_r = A_{2g} + T_{1g} + T_{2g}$, or $\Gamma_r = \Gamma_2^+ + \Gamma_4^+ + \Gamma_5^+$ using Bethe's notation. The term splits into seven levels, one of symmetry A_2 (or A_{2g}), three degenerate ones of symmetry T_1 (or T_{1g}) and three of symmetry T_2 (or T_{2g}), consistent with the $2J + 1 = 7$ degeneracy of the parent term. A similar exercise for the $^5D_0$ term shows that its $\Gamma_r = \Gamma_1^+$. Inspection of the multiplication tables indicates that the only transitions allowed are the magnetic dipole transitions, which occur between terms with irreducible representation, which contain the O_{MD}, as required by Equation 1.54 and shown in Table 1.14. Therefore the $^5D_0 - {}^7F_1$ transition has a magnetic dipole allowed component. Other transitions are observed for Eu(III) nonetheless, and those include induced electric dipole transitions, which will be discussed in the following paragraph.

Complete multiplication tables can be found in the literature [30].

Similarly, it can be shown that the $^2F_{5/2}$ term of Yb(III) transforms in D_3 as the reducible representation Γ_r displayed in Table 1.15.

Table 1.15 *Reducible representation of the $^2F_{5/2}$ term of Yb(III) in D_3 symmetry*

D_3' [a]	E	R	C_3	C_3^2	$3C_2$	$3C_2R$
			C_3^2R	C_3R		
Γ_r	6	−6	0	0	0	0

[a] The double group D_3' is used instead of D_3, as Yb(III) is a Kramer's ion.

Table 1.16 *Multiplication table showing the selection rules for the D_3' point group [30]*

D_3'	ED		MD	
	Γ_4	$\Gamma_{5,6}$	Γ_4	$\Gamma_{5,6}$
Γ_4	α, π, σ	α, σ	α, σ, π	α, π
$\Gamma_{5,6}$	α, σ	π	α, π	σ

After reduction $\Gamma_r = 2\Gamma_4 + \Gamma_{5,6}$, which corresponds to two doubly degenerate levels with symmetry Γ_4 and two degenerate levels with symmetries Γ_5 and Γ_6, consistent with an overall sixfold degeneracy which is not completely lifted by the crystal field, as Yb(III) is a Kramers' ion. Analogously, the $^2F_{7/2}$ term transforms as the reducible representation $\Gamma_r = 3\Gamma_4 + \Gamma_{5,6}$.

Inspection of Table 1.16 above shows that transitions between these two terms are both electric and magnetic dipole allowed as well as polarised, since they are allowed only in certain directions. The transition between levels with $\Gamma_{5,6}$ symmetry is allowed only in π polarised spectra. A π-polarised spectrum is measured with the magnetic field perpendicular and the electric field parallel to the crystallographic c axis. An α-spectrum, on the other hand, is measured with both the magnetic and electric field vectors perpendicular to the crystallographic c axis. Measurement of the σ-spectrum occurs with the magnetic field parallel and the electric field perpendicular to the c axis. Polarised spectra yield useable results only in uniaxial crystals, which have trigonal, tetragonal and hexagonal unit cells.

1.3.9.5 Intensity of the MD Transitions

The magnetic dipole strength of a transition between the initial and final states ψ_i and ψ_f can be theoretically evaluated by determining the matrix elements of the dipole moment operator O_{MD} coupling the two states [40]. By re-writing Equation 1.56 without the summation over all i electrons, O_{MD} is given by

$$O_{MD} = -\frac{e\hbar}{2m_e c}(\hat{L} + 2\hat{S}) \tag{1.59}$$

Therefore, the strength of the magnetic dipole transition D_{MD} is given by Equation 1.60.

$$D_{MD} = \left\langle \psi_i \middle| O_{MD} \middle| \psi_f \right\rangle^2 = \frac{e^2\hbar^2}{4m_e^2c^2}\left| \left\langle l^N SLJ \middle| O_{MD} \middle| l^N S'L'J' \right\rangle^2 \right. \tag{1.60}$$

After separating the quadratic term into expressions containing individually the total orbital angular momentum operator $\hat{L}$ and the total spin angular momentum operator $\hat{S}$, it can be shown that [55]

$$\begin{aligned}
\left\langle l^N SLJ \middle| \hat{L} \middle| l^N S'L'J' \right\rangle &= \delta_{SS'}\delta_{LL'}(-1)^{S+L+J+1}\begin{Bmatrix} L & J & S \\ J & L & 1 \end{Bmatrix}[(2L+1)(2J+1)^2L(L+1)]^{1/2} \\
\left\langle l^N SLJ \middle| \hat{S} \middle| l^N S'L'J' \right\rangle &= \delta_{SS'}\delta_{LL'}(-1)^{S+L+J+1}\begin{Bmatrix} S & J & L \\ J & S & 1 \end{Bmatrix}[(2S+1)(2J+1)^2S(S+1)]^{1/2}
\end{aligned} \tag{1.61}$$

Therefore, for MD transitions the following selection rules arise.

$$\Delta S = 0$$

$$\Delta L = 0$$

$$\Delta J = 0, \pm 1, \text{ but } 0 \leftrightarrow 0 \text{ forbidden}$$

As there are three possible values for ΔJ, it can be shown that for:

1. $\Delta J = 0$, $J = J'$ and

$$\left\langle l^n SLJ \middle| \hat{L} + 2\hat{S} \middle| l^n S'L'J' \right\rangle = g[J(J+1)(2J+1)]^{1/2}$$

$$g = 1 + \frac{J(J+1) - L(L+1) + S(S+1)}{2J(J+1)}$$

g, the Landé factor, describes the magnetic moment of the ion.

2. $J' = J - 1$

$$\left\langle l^n SLJ \middle| \hat{L} + 2\hat{S} \middle| l^n S'L'(J-1) \right\rangle = \left[\frac{1}{4J}(S+L+J+1)(S+L+J-1)(J+S-L)(J+L-S)\right]^{1/2}$$

3. $J' = J + 1$

$$\left\langle l^n SLJ \middle| \hat{L} + 2\hat{S} \middle| l^n S'L'(J+1) \right\rangle = \left[\frac{1}{4J+1}(S+L+J+2)(S+J+1-L)(L+J+1-S)(S+L-J)\right]^{1/2}$$

Representative values for dipole and oscillator strengths for selected MD allowed Ln(III) transitions are summarised in Table 1.17.

Since MD allowed transitions are relatively independent of the geometry surrounding the lanthanide ions, both ligand identity as well as coordination polyhedra do not influence transition intensity appreciably.

Table 1.17 *Dipole D and oscillator P strengths for MD allowed transitions for select Ln(III)*

Ln(III)	MD allowed transition	E [cm^{-1}]	P_{MD} [10^{-8} Debye^2][a]	D_{MD} [10^{-6} Debye^2]
Pr(III)	$^3H_5 \leftarrow {}^3H_4$	2300	9.76	90
Nd(III)	$^4I_{11/2} \leftarrow {}^4I_{9/2}$	2000	14.11	15
Eu(III)	$^5D_0 \leftarrow {}^7F_1$	16 900	7.47	9.4

[a] 1 Debye = 1×10^{-18} esu cm

1.3.10 Induced Electric Dipole Transitions and Their Intensity – Judd–Ofelt Theory

Since the electric dipole operator has odd parity, electric dipole transitions are allowed only between states of different parity, as mentioned before. Therefore, the electric dipole operator must be combined with other odd-parity operators to enable transitions within the *f* shell [56]. If the metal is present in a symmetry site without inversion symmetry, the parity rule is no longer applicable and therefore electric dipole transitions can be observed. However, even in centrosymmetric point groups, electric dipole transitions can be observed, as vibronic coupling, which is coupling of the electronic and vibrational wave functions, lifts the site symmetry. Alternatively, admixture of electronic states of opposite parity, such as *d* orbitals, mediated by the crystal field, which was proposed concurrently and independently by Brian Judd [8] and George Ofelt [9], can be invoked to explain the intensity of these transitions. While arbitrary, a small participation of the *d* orbitals can be seen as a small perturbation to the system, which results in new perturbed wave functions φ_a and φ_b for the initial and final states, where the wave functions ψ designated with α and β correspond to the orbitals of higher energy with opposite parity.

$$\langle \varphi_a | = \langle \psi_a | + \sum_{\beta} \frac{\langle \psi_a | H_{cf} | \psi_\beta \rangle}{E_a - E_\beta} \langle \psi_\beta |$$

$$| \varphi_b \rangle = | \psi_b \rangle + \sum_{\beta} \frac{\langle \psi_\beta | H_{cf} | \psi_b \rangle}{E_b - E_\beta} | \psi_\beta \rangle$$

By utilising these new wave functions, the dipole strength D_{ED} of the line corresponding to the transition between the states *a* and *b* is given by Equation 1.62.

$$\begin{aligned} D_{ED} &= \langle \varphi_a | O_{ED} | \varphi_b \rangle^2 \\ &= \left[\sum_{\beta} \left\{ \frac{\langle \psi_a | H_{cf} | \psi_\beta \rangle \langle \psi_\beta | O_{ED} | \psi_b \rangle}{E_a - E_\beta} + \frac{\langle \psi_a | O_{ED} | \psi_\beta \rangle \langle \psi_\beta | H_{cf} | \psi_b \rangle}{E_b - E_\beta} \right\} \right]^2 \end{aligned} \tag{1.62}$$

In this expression, since O_{ED} is odd-parity and the states *a* and *b* have opposite parity to α and β, those terms will not vanish. To prevent the terms involving the crystal field Hamiltonian from vanishing, the B_q^k parameters have to be odd, with $k = 1, 3, 5$ and $q \leq k$. The crystal field operator H_{cf} and electric dipole operator O_{ED} can be re-written as shown below.

$$H_{cf} = \sum_i r_i C_q^1(\theta_i, \phi_i) \tag{1.63}$$

$$O_{ED} = \sum_{t,p} A_p^t \sum_i r_i^t (C_p^t)_i \tag{1.64}$$

C_q^k are the tensor operators introduced in Equation 1.31, which transform like the spherical harmonics.

Substitution of these expressions into Equation 1.62 leads to Equation 1.65.

$$D_{ED} = \left[\sum_{p,t,\text{ even } \lambda} (-1)^{J-M_J+p+q}(2\lambda+1)A_p^t \begin{pmatrix} 1 & \lambda & t \\ q & -p-q & p \end{pmatrix} \begin{pmatrix} J & \lambda & J' \\ -M_J & -p-q & M_{J'} \end{pmatrix} \begin{Bmatrix} 1 & \lambda & t \\ l & l' & l \end{Bmatrix} \times \langle \psi_a \| U^\lambda \| \psi_b \rangle \times \Xi(t,\lambda) \right]^2$$

with

$$\Xi(t,\lambda) = 2\sum_{nl}(2l+1)(2l'+1)(-1)^{l+l'} \times \begin{Bmatrix} 1 & \lambda & t \\ l & l' & l \end{Bmatrix} \begin{pmatrix} l & 1 & l' \\ 0 & 0 & 0 \end{pmatrix} \begin{pmatrix} l & t & l' \\ 0 & 0 & 0 \end{pmatrix} \times \frac{(nl|r|n'l')(nl|r^t|n'l')}{\Delta E_{nl}} \tag{1.65}$$

In this expression $\lambda = 1 + t$, t is odd, $A_p^t = \frac{B_p^t}{\langle r \rangle^t}$ (Equation 1.29) are the static crystal field parameters, with $t \to k$ and $p \to q$ and, for the $3j$ and $6j$ symbols to be different from zero and therefore the dipole moment does not vanish, the following parameter values and selection rules arise for induced electric dipole transitions:

$$\lambda = 2, 4, 6$$

$$t = 1, 3, 5$$

$$\Delta J \leq 6 \,(\text{no } 0 \leftrightarrow 0)$$

$$\Delta J = 2, 4, 6 \text{ when } J \text{ or } J' = 0, \text{ otherwise } \Delta J = 0, \pm 1$$

$$\Delta L \leq 6$$

$$\Delta S = 0$$

Following some simplifications, such as the assumption that all Stark levels of the ground state manifold are equally populated, and that the emission is isotropic, the dipole strength can be simplified to Equation 1.66.

$$D_{ED} = e^2 \sum_{\lambda=2,4,6} \Omega_\lambda \left| \langle \psi_a \| U^\lambda \| \psi_b \rangle \right|^2 \tag{1.66}$$

U^λ are the tensors of the electric dipole operator of rank $\lambda = 2, 4, 6$, and the terms in brackets are the doubly reduced matrix elements for intermediate coupling, which have been determined by Carnall for all lanthanide aqua ions [25–28]. Some are summarised in Table 1.18.

Ω_λ are the Judd–Ofelt parameters in cm^{-1} [8,9,55].

$$\Omega_\lambda = (2\lambda+1)\sum_p \sum_{t=1,3,5} \frac{|A_p^t|^2}{(2t+1)} \Xi^2(t,\lambda) \tag{1.67}$$

Table 1.18 *Selected squares of doubly reduced matrix elements* $\left|\langle\psi_a\|U^{\lambda}\|\psi_b\rangle\right|^2$ *for Eu(III) [26]*

	$\lambda=2$	$\lambda=4$	$\lambda=6$
$^7F_0 \rightarrow$			
$^5D_0$	0	0	0
$^5D_1$	0	0	0
$^5D_2$	0.0008	0	0
$^5L_6$	0	0	0.0155
$^7F_1 \rightarrow$			
$^5D_0$	0	0	0
$^5D_1$	0.0026	0	0
$^5D_2$	0.0001	0	0
$^5L_6$	0	0	0.0090

The expression above shows that odd-order components of the crystal field and radial integrals of $4f^n$ wavefunctions and of perturbing wavefunctions of opposite parity comprise these parameters. These parameters appear in the definition of the oscillator strength P_{ED} for a particular induced electric dipole transition between and a and b, as shown in the equation below [57].

$$P_{ED}(a \leftrightarrow b) = \frac{8\pi^2 m_e \nu (n^2+2)^2}{27hn(2J+1)} \sum_{\lambda=2,4,6} \Omega_\lambda \left|\langle\psi_a\|U^{\lambda}\|\psi_b\rangle\right|^2 \tag{1.68}$$

The Judd–Ofelt parameters can, in principle, be calculated; however, it is more common to treat them as phenomenological parameters, which can be fitted from absorption or emission spectra, through measurement of the experimental dipole strength as defined in Equation 1.48 and the use of the tabulated doubly reduced matrix elements with Equation 1.68. The Judd–Ofelt parameters, as determined experimentally, are often given in units of $10^{-20}\,\mathrm{cm}^2$. Ω_2 is strongly affected by dynamic coupling between the ligands and the lanthanide ion, which is related to changes in the ligand-generated field due to the incident light. This changing field in turn induces *f-f* transitions. Ω_6 is strongly influenced by the rigidity of the host the lanthanide is embedded in. In this static coupling model, the ligands generate a crystal field potential of odd parity, which in turn induce 4*f* states of mixed parity. The electric dipole component of the incident photons then induces transitions between these states, but the ligands themselves are not affected by the incident radiation. The Ω_4 parameters do not show specific trends and involve both dynamic and static coupling mechanisms [57,58]. In general, if the host matrix is the same and the lanthanide ions are in isostructural positions, a decrease of the Ω_λ parameters along the series is expected, and is indeed observed for Ω_6, due to static coupling prevalence (Tables 1.19 and 1.20). In the case of Ω_4, the trend is less consistent, and, for Ω_2 no trend is observed, as dynamic coupling is prevalent.

The Judd–Ofelt theory does not estimate well transition intensities for Pr(III), as it is likely that the $4f^15d^1$ configuration contributes significantly to the perturbation described in φ_a and φ_b.

Table 1.19 *Judd–Ofelt parameters for aqueous Ln(IIII) ions in acidic solutions [31]*

Ln	Ω_2 [10^{-20} cm^2]	Ω_4 [10^{-20} cm^2]	Ω_6 [10^{-20} cm^2]
Pr	32.6	5.7	32.0
Nd	0.93	5.00	7.91
Sm	0.91	4.13	2.70
Eu	1.46	6.66	5.40
Gd	2.56	4.70	4.73
Tb	0.004	7.19	3.45
Dy	1.50	3.44	3.46
Ho	0.36	3.14	3.07
Er	1.59	1.95	1.90
Tm	0.80	2.08	1.86

Table 1.20 *Judd–Ofelt parameters for Nd(III) in selected environments [57]*

Nd	Ω_2 [10^{-20} cm^2]	Ω_4 [10^{-20} cm^2]	Ω_6 [10^{-20} cm^2]
Aqua	0.93 ± 0.3	5.0 ± 0.3	7.9 ± 0.4
Nitrate	9.2 ± 0.4	5.4 ± 0.3	7.7 ± 0.45
Acetylacetonate in DMF	24.5	0.71	9.1
Acetylacetonate in MeOH/EtOH	15.7	0.73	7.4
Dibenzoylacetonate in MeOH/EtOH	34.1	2.5	9.1
Bromide	180	9	9
Iodide	275	9	9
YAG	0.2	2.7	5.0

1.3.11 Transition Probabilities and Branching Ratios

The probability of an individual transition $J \leftrightarrow J'$ to occur is given by Equation 1.69.

$$A(J,J') = \frac{64\pi^4 e^2 \bar{\nu}^3}{2h(2J+1)} \left[\chi_{ED} D_{ED} + \chi_{MD} D_{MD}\right] \tag{1.69}$$

The correction factors for dielectric medium, χ, used in this equation will depend on the transitions being absorption or emission. Further, since individual transitions will have different probabilities, it is possible to define a radiative branching ratio $\beta_R(J,J')$, given by Equation 1.70.

$$\beta_R(J,J') = \frac{A(J,J')}{\sum_J A(J,J')} = \frac{E(J,J')}{\sum_J E(J,J')} \tag{1.70}$$

The radiative branching ratio can be calculated through the probabilities of the transitions, or, in the case of emission, it can be determined experimentally from the emission spectra, where $E(J,J')$ is the integrated emission spectrum of transition $J \leftrightarrow J'$ and $\sum_J E(J,J')$ is the integrated emission spectrum over all transitions.

In the case of emission, $A(J,J')$ is also known as Einstein's coefficient of spontaneous emission, and the sum of all probabilities for all radiative transitions is equal to the inverse of the radiative rate constant, k_R, in turn the reciprocal of the emissive state lifetime, τ_R.

$$\beta_R(J,J') = \frac{A(J,J')}{\sum_J A(J,J')} = \frac{A(J,J')}{k_R} = \tau_R A(J,J') \tag{1.71}$$

Werts and co-workers [59] demonstrated that for the purely magnetic dipole transition of Eu^{3+}, $^5D_0 \rightarrow {}^7F_1$, the equation above can be rearranged to

$$\frac{1}{\tau_R} = A(^5D_0 \rightarrow {}^7F_1)n^3\left(\frac{E(^5D_0 \rightarrow {}^7F_J)}{E(^5D_0 \rightarrow {}^7F_1)}\right) \tag{1.72}$$

and $A(^5D_0 \rightarrow {}^7F_1) = 14.65\ s^{-1}$ is the spontaneous emission probability of the purely magnetic dipole transition *in vacuo*, which was calculated through Equation 1.69 above.

For other lanthanide ions, Equation 1.72 can be re-written as Equation 1.73.

$$\frac{1}{\tau_R} = 2303\frac{8\pi cn^2\overline{\nu}^2}{N_A}\frac{(2J+1)}{(2J'+1)}\int \varepsilon(\overline{\nu})d\overline{\nu} \tag{1.73}$$

$\int \varepsilon(\overline{\nu})d\overline{\nu}$ is the integrated absorption spectrum of the transition in molar absorptivity as a function of wavenumber.

Werts and co-workers tested the validity of these calculations by comparing experimental and calculated parameters for well-studied systems, the europium salts of dipicolinic acid [59]. They found an error of about 15% between experimentally determined and calculated branching ratios and radiative lifetimes.

1.3.12 Hypersensitive Transitions

Hypersensitive transitions are electric dipole transitions whose shape and intensity display large dependence on the point group symmetry of the metal ion, as well as on the pH, temperature, and ligand type. These transitions obey the following selection rules.

$$\left|\Delta S\right| = 0 \qquad \left|\Delta L\right| \leq 2 \qquad \left|\Delta J\right| \leq 2$$

Table 1.21 below summarises hypersensitive transitions observed for the different lanthanides. These transitions are usually observed for systems that display large values of U^2 and therefore Ω_2 and comparatively small and symmetry-independent values of Ω_4 and Ω_6 [13].

While over the years several explanations have been proposed for hypersensitivity, including symmetry arguments, vibronic, charge-transfer and electric-quadrupole transition contributions [57,58], the most successful to date has been the dynamic coupling mechanism proposed by Mason et al. [60]. These authors suggest that the intensity of the hypersensitive transitions results from a non-zero electric dipole transition, which arises from an electric dipole in the ligand induced by the *f* orbitals of the metal ion. By analogy

Table 1.21 *Hypersensitive transitions of the Ln(III) ions observed in absorption or emission spectra [13,57]*

Ln(III)	Transition	λ [nm]
Pr	$^3F_2 - {}^3H_4$	1920
Nd	$^4G_{5/2} - {}^4I_{9/2}$	578
	$^2H_{9/2}, {}^4F_{5/2} - {}^4I_{9/2}$	806
	$^4G_{7/2}, {}^3K_{13/2} - {}^4I_{9/2}$	521
Sm	$^4F_{1/2}, {}^4F_{3/2} - {}^6H_{5/2}$	1560
Eu	$^5D_2 - {}^7F_0$	465
	$^5D_1 - {}^7F_1$	535
	$^5D_0 - {}^7F_2$	613
Gd	$^6P_{5/2}, {}^6P_{7/2} - {}^8S_{7/2}$	308
Dy	$^6F_{11/2} - {}^6H_{15/2}$	1300
	$^4G_{11/2}, {}^4I_{15/2} - {}^6H_{15/2}$	427
Ho	$^3H_6 - {}^5I_8$	361
	$^5G_6 - {}^5I_8$	452
Er	$^4G_{11/2} - {}^4I_{15/2}$	379
	$^2H_{11/2} - {}^4I_{15/2}$	521
Tm	$^1G_4 - {}^3H_6$	469
	$^3H_4 - {}^3H_6$	787
	$^3F_4 - {}^3H_6$	1695

with Equation 1.62 it is possible to write Equation 1.74 for the electric dipole moment μ.

$$\langle A_0 B_0|\mu|A_a B_0\rangle = \sum_b \frac{2E_b}{(E_b^2 - E_a^2)} \langle A_0 A_a|V|B_0 B_b\rangle \mu_{0b} \tag{1.74}$$

$\langle A_0|$ and $|Aa\rangle$ are the ground and excited states of the metal ion, respectively, which perturb the $\langle B_0|$ ground and $|B_b\rangle$ excited states of the ligand. μ_{0b} is the electric dipole moment of the ligand transition influenced by the Coulombic interaction V between the f orbitals and the ligand B. The dynamic coupling contributes then to the Ω_2 Judd–Ofelt parameter, if the crystal field potential has crystal field terms with k odd ($k = 3$).

1.3.13 Emission Efficiency and Rate Constants

The emission efficiency is given by the quantum yield of luminescence ϕ, which is simply the ratio of emitted photons, p_{em}, to photons absorbed by the sample, p_{abs}, as shown in Equation 1.75.

$$\phi = \frac{p_{em}}{p_{abs}} \tag{1.75}$$

In the case of lanthanides, following direct excitation of the metal ion, the efficiency of emission is called the intrinsic emission efficiency ϕ_{Ln}^{Ln}, which is directly related to the overall rate at which the emissive state is depopulated through radiative *R* and non-radiative *NR* pathways, $k_{exp} = k_R + k_{NR}$, and the radiative rate constant, k_R, or their corresponding lifetimes, τ_{exp} and τ_R, as shown in Equation 1.76.

$$\phi_{Ln}^{Ln} = \frac{k_R}{k_R + k_{NR}} = \frac{k_R}{k_{exp}} = \frac{\tau_{exp}}{\tau_R} \tag{1.76}$$

The experimentally observed excited state lifetime reflects the contribution of all processes, which lead to the deactivation of the excited state, both radiative and non-radiative.

Equation 1.72 above relates the radiative lifetime to the magnetic dipole-allowed transition of Eu(III). It is therefore straightforward to determine experimentally, for this ion, τ_R and therefore the intrinsic emission efficiency.

1.4 Sensitisation Mechanism

1.4.1 The Antenna Effect

Due to the forbidden nature of the *f-f* transitions, for many applications the direct excitation of the lanthanide ion is not desirable, as it requires the use of high intensity sources. It is therefore more efficient to promote the emission through an appended sensitiser or antenna. The antenna effect, illustrated in Fig. 1.10, relies on a sensitiser to harvest energy, for example through photon absorption, which leads to population of an excited single state ^{1}S. In the presence of a heavy atom, intersystem crossing ISC is facilitated, which leads to population of a triplet excited state ^{3}T. This state is usually long-lived and is capable therefore of energy transfer ET to the lanthanide ion's emissive f^* excited state. If the emissive state is too close in energy to the triplet state, back energy transfer BT occurs.

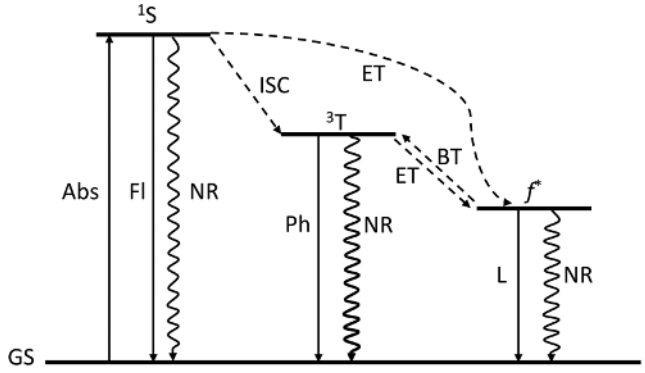

Figure 1.10 *Modified Jablonski diagram illustrating the antenna effect. Abs – absorption, Fl – fluorescence, Ph – phosphorescence, L – luminescence, ISC – intersystem crossing, ET – energy transfer, BT – back energy transfer, NR – non-radiative deactivation, ^{1}S – first excited singlet state, ^{3}T – lowest excited triplet state, GS – ground state, f* – emissive* f *excited state*

Fluorescence Fl and phosphorescence Ph compete for deactivation of the singlet and triplet states, respectively, and non-radiative processes NR can also lead to deactivation of all excited states. Although it is usually assumed that the energy transfer occurs from the triplet excited state due to the favourable intersystem crossing in the presence of the heavy atom [61], several cases have been reported in which the energy is transferred from the singlet excited state directly to the emissive *f* level [62–66]. It has also been shown that sensitisation through metal to ligand charge-transfer states of coordinated transition metal complexes or intra-ligand charge-transfer states are viable pathways to promote lanthanide-centred emission [67].

The overall efficiency of sensitised emission ϕ_{Ln}^{L} is given by Equation 1.77.

$$\phi_{Ln}^{L} = \phi_{ISC} \times \phi_{ET} \times \phi_{Ln}^{Ln} = \phi_{sens} \times \phi_{Ln}^{Ln} \tag{1.77}$$

The efficiency of intersystem crossing ϕ_{ISC} and efficiency of energy transfer ϕ_{ET} combine to give the efficiency of sensitisation ϕ_{sens}. In the case of europium, where τ_r (Equation 1.72) can be obtained from the integrated emission spectrum and ϕ_{Ln}^{Ln} can be estimated with Equation 1.76, it is therefore possible to experimentally determine the efficiency of sensitisation ϕ_{sens}.

1.4.1.1 Singlet and Triplet States and Intersystem Crossing

The relative positions of the singlet and triplet states are important, as they can help influence the efficiency of the intersystem crossing as well as the energy transfer and magnitude of back energy transfer. Work done by Latva et al. [68] indicates that the position of the lowest triplet state relative to the emissive state of the Ln(III) ion is important for the efficiency of the energy transfer. From their survey of 41 different ligands, these authors conclude that for Eu(III) good energy transfer happens if the triplet to *f** gap is in the range 2500–4000 cm^{-1}, with emission efficiencies in the range 15–38%. Nonetheless, an emission efficiency of 12% was observed for a complex with $\Delta E \approx 9000\,cm^{-1}$, and an emission efficiency of 11% was observed for another complex with $\Delta E \approx 1000\,cm^{-1}$. In the case of Tb(III), emission efficiencies in the range 21–58% were observed for ΔE in the range 2000–4300 cm^{-1}. For this metal ion, with its emissive $^5D_4$ state at 20 450 cm^{-1}, substantial energy back-transfer was observed if $\Delta E \leq 1850\,cm^{-1}$.

In the course of the pioneering work on sensitised luminescence, Yuster and Weissman studied the promotion of intersystem crossing due to spin–orbit coupling with heavy atoms [69]. They found that dibenzoylmethanide coordinated to the non-emissive La, Lu and Gd displayed different efficiencies of intersystem crossing, as seen by different ratios of fluorescence versus phosphorescence intensity and changes in phosphorescence lifetimes, directly related to spin–orbit coupling and to the magnetic moment of the lanthanide ion.

The lifetime $\tau(^1S)$ of the singlet excited state is given by Equation 1.78.

$$\tau(^1S) = \frac{1}{k_{NR} + k_{Fl} + k_{ISC}} \tag{1.78}$$

k_{NR} is the non-radiative decay rate, while k_{Fl} is the radiative decay rate and k_{ISC} the rate of intersystem crossing (see Fig. 1.10). The lifetime $\tau(^3T)$ of the triplet excited state is

given by Equation 1.79.

$$\tau(^3T) = \frac{1}{k'_{NR} + k_{Ph}} \tag{1.79}$$

k'_{NR} is the non-radiative decay from the triplet state back to the singlet ground state and k_{Ph} is the radiative phosphorescence decay rate.

The emission efficiencies for the fluorescence ϕ_{Fl} and phosphorescence ϕ_{Ph} can then be defined by Equations 1.80 and 1.81, respectively.

$$\phi_{Fl} = \frac{k_{Fl}}{k_{NR} + k_{ISC} + k_{Fl}} \tag{1.80}$$

$$\phi_{Ph} = \frac{k_{Ph} + k_{ISC}}{(k_{NR} + k_{Ph})_{Ph}(k_{ISC} + k_{Fl} + k_{NR})_{Fl}} \tag{1.81}$$

1.4.1.2 Ligand to Metal Ion Energy Transfer Mechanisms

As mentioned above, sensitised luminescence is the process by which lanthanide ions emit following absorption of light by a coordinated ligand. During this process the absorbed energy has to be transferred to the lanthanide ion. In general, energy transfer between a donor *D* and an acceptor *A* will follow one of two mechanisms, one involving electron transfer, also called Dexter energy transfer [70], and the other involving dipole–dipole exchange, also known as Förster energy transfer [71], represented in Fig. 1.11 [72].

Due to the lack of overlap of the 4*f* orbitals with the ligand orbitals, it is generally accepted that the energy transfer occurs through the latter for lanthanide ions and so only the Förster mechanism will be briefly discussed in the following. However, in the case of lanthanide ions such as europium and ytterbium, which are easily reduced, electron transfer and phonon-assisted mechanisms have been invoked [73,74].

Förster or Dipole–Dipole Energy Transfer For systems in which molecules are present that are capable of absorbing and emitting energy and energy transfer is observed between donors and acceptors, Förster postulated that the decrease in excitation of the donor occurs in parallel with the increase in emission of the acceptor, which is consistent with a dipole–dipole exchange mechanism. This is different from a sequential process in which the donor emits and its emission wavelengths are reabsorbed by the acceptor [71].

When donors and acceptors are present in the system and the former are de-excited while the latter absorb energy, the rate constant for energy transfer $k_{D\text{-}A}$ between donor *D* and acceptor *A* is given by Equation 1.82.

$$k_{D-A} = \frac{161.9\ \kappa^2}{\pi^6 n^4 N \tau_0 R^6} \int_0^\infty f_D(\nu)\varepsilon_A(\nu)\frac{d\nu}{\nu^4} = \frac{161.9\ \kappa^2}{\pi^6 n^4 N \tau_0 R^6} J(\nu) \tag{1.82}$$

R is the distance between donor *D* and acceptor *A*, *n* is the refractive index of the solution, τ_0

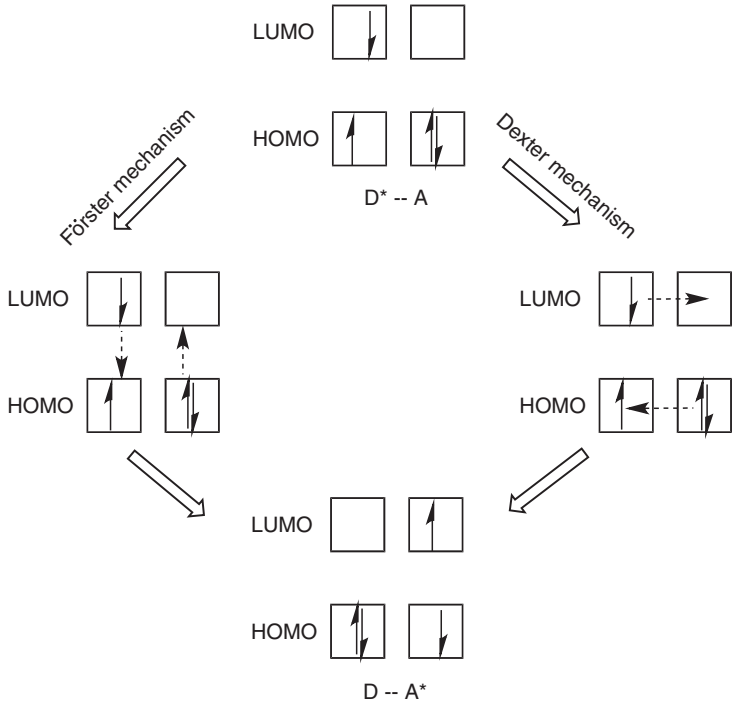

Figure 1.11 *Pictorial representation of energy transfer between donor* D *and acceptor* A *through the Förster and Dexter mechanisms*

is the natural radiative lifetime of the donor in absence of the acceptor and N is Avogadro's number. The overlap integral $J(\nu)$ is determined through integration of the absorption spectrum of the acceptor $\varepsilon_A(\nu)$, in units of cm^{-1} M^{-1}, and the emission spectrum of the donor $f_D(\nu)$, in units of cm^{-1}, normalised to an area of 1.0. Finally, since dipole–dipole interactions depend on molecular orientation, the orientation factor κ is present in this equation [71]. For solutions in which molecular positions are averaged due to random motion, κ^2 is usually equal to two-thirds [75]. From this equation it follows that the energy transfer depends on R^{-6}, and therefore Förster energy transfer is a long-range interaction which requires overlap of emission spectrum of the donor and absorption spectrum of the acceptor, but does not require physical contact between the donor and acceptor. The Förster distance R_0, which is the maximum donor–acceptor distance for which energy transfer is possible, is given by Equation 1.83 [71].

$$R_0 = \sqrt[6]{\frac{3000\tau_0 c^2 J(\nu)}{8\pi^4 n^2 N^2 \nu_0^2}} \tag{1.83}$$

Here, c is the speed of light in a vacuum and ν_0 is the frequency at which absorption and emission spectra intersect.

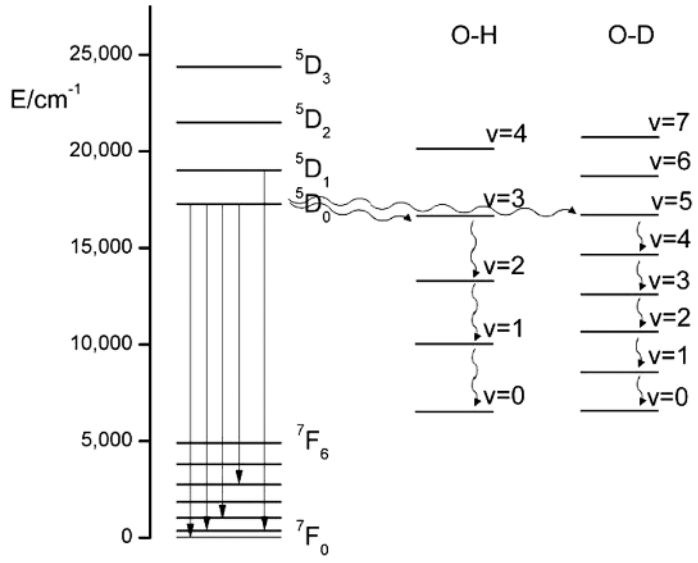

Figure 1.12 *Radiative transitions of Eu(III) and non-radiative quenching through O–H and O–D bonds*

1.4.2 Non-Radiative Quenching

As shown in Fig. 1.11, non-radiative quenching pathways are present at several places of the sensitisation process and lead to overall low emission efficiency of sensitised emission. In the case of intrinsic Ln(III) ion emission, the smaller the gap between the emissive state and the highest sublevel of the ground-state manifold, the easier it is to non-radiatively quench the emission. This is shown in Fig. 1.12 for Eu(III), where the gap between the $^5D_0$ and the $^7F_6$ states is approximately 12 000 cm^{-1}. It follows that the quenching of the emissive state is easily accomplished through three vibrational quanta of the O–H bond, with a vibrational energy of 3600 cm^{-1}. If instead the bond is O–D, with a vibrational energy of 2200 cm^{-1}, five vibrational quanta are needed, and the process is less efficient.

Table 1.22 summarises the number of phonons necessary to bridge the gap ΔE between an excited Ln(III) state and the highest energy sub-level of the ground-state manifold for H_2O and D_2O.

Table 1.22 *Vibrational bridging of the ΔE gap for different Ln(III) ions by O–H and O–D bonds and typical radiative lifetimes τ*

		Number of phonons		τ [ms]	
Ln	ΔE [cm^{-1}]	OH	OD	H_2O	D_2O
Gd	32 100	9	15	2.3	n.a.
Tb	14 800	4	7	0.47	3.8
Eu	12 300	3–4	5–6	0.11	4.1
Dy	8850	2–3	3–4	0.002	0.06
Sm	7400	2	3	0.002	0.08

Horrocks and co-workers took advantage of this and derived an empirical equation, which allows the determination of the number of water molecules coordinated to Eu(III) and Tb(III) by comparing emission lifetimes in water and deuterated water. This will be further discussed in Chapter 2 [76,77].

In addition to O−H other bonds, such as N−H (3300 cm^{-1}) and C−H (2900 cm^{-1}), also contribute to vibrational quenching of Ln(III)-centred emission.

Since the non-radiative quenching processes are vibrationally mediated, they are temperature dependent and the temperature dependence of the rate constants is described by an Arrhenius-like Equation 1.84.

$$\ln\left(k_{exp} - k_0\right) = \ln A - \frac{E_A}{RT} \tag{1.84}$$

k_0 is the rate constant at 0 K, which can be approximated by the rate constant measured experimentally at 4 K or 77 K and E_A is the activation energy for the quenching process. This can be used, for example, to determine the activation energy for energy back-transfer from the emissive Ln(III) state to the triple state. Charbonnière et al. determined an activation energy of 180 cm^{-1} for the back-transfer from the $^5D_4$ level of Tb(III) to the triplet state of a calixarene located at 2400 cm^{-1} [78]. The authors hypothesise that the back-transfer is mediated by Ln–O vibrations in the complex, which occur at around 220 cm^{-1}.

Acknowledgement

Support through the National Science Foundation grant CHE-1058805 is gratefully acknowledged.

Abbreviations

^1S	first excited singlet state
^3T	lowest excited triplet state
A	acceptor
AOM	angular overlap model
BT	back energy transfer
CN	coordination number
D	donor
ED	electric dipole
ET	energy transfer
Fl	fluorescence
GS	ground state
ISC	intersystem crossing
L	luminescence
Ln	lanthanide
MD	magnetic dipole
NR	non-radiative

PCEM point charge electrostatic model
Ph phosphorescence
R radiative
SOM simple overlap model

References

1. Evans, C. H. (ed.) *Episodes from the History of the Rare Earth Elements;* Cambridge Unversity Press: Cambridge, **1996**.
2. Kirchhoff, G.; Bunsen, R. *Quart. J., Chem. Soc., London* **1861**, *13*, 270–289.
3. von Welsbach, C. A. *Justus Liebigs Ann., Chem.* **1907**, *351*, 458–466.
4. von Welsbach, C. A. *Monatsh. Chem.* **1883**, *4*, 630–642.
5. von Welsbach, C. A. *Monatsh. Chem.* **1884**, *5*, 508–522.
6. Condon, E. U.; Shortley, G. H. *The Theory of Atomic Spectra;* Cambridge Unversity Press: Cambridge, **1996**.
7. Van Vleck, J. H. *J. Phys. Chem.* **1937**, *41*, 67–80.
8. Judd, B. R. *Phys. Rev.* **1962**, *127*, 750–761.
9. Ofelt, G. S. *J. Chem. Phys.* **1962**, *37*, 511–520.
10. Weissman, S. I. *J. Chem. Phys.* **1942**, *10*, 214–217.
11. Bünzli, J.-C. G.; Choppin, G. R. (eds) *Lanthanide Probes in Life, Chemical and Earth Sciences – Theory and Practice;* Elsevier: Amsterdam, **1989**.
12. Bünzli, J. C. G. In *Spectroscopic Properties of Rare Earths in Optical Materials;* Liu, G., Jacquier, B., (eds); Springer: Berlin, 2005; Vol. 83, pp. 462–499.
13. Sastri, V. S.; Bünzli, J. C.; Perumareddi, J. R.; Rao, V. R.; Rayudu, G. V. S. (eds) *Modern Aspects of Rare Earths and Their Complexes* Elsevier: Amsterdam, **2003**.
14. Huheey, J. E.; Keiter, E. A.; Keiter, R. L. *Inorganic Chemistry: Principles of Structure and Reactivity;* 4th edn; Harper Collins: New York, **1993**.
15. Reddy, J. V. *Symmetry and Spectroscopy of Molecules;* New Age Science: Maidstone, **2010**.
16. Dieke, G. H. *Spectra and Energy Levels of Rare Earth Ions in Crystals;* Interscience: New York, **1968**.
17. Dieke, G. H.; Sarup, R. *J. Chem. Phys.* **1958**, *29*, 741–745.
18. Varsanyi, F.; Dieke, G. H. *J. Chem. Phys.* **1962**, *36*, 2951–2961.
19. Thomas, K. S.; Singh, S.; Dieke, G. H. *J. Chem. Phys.* **1963**, *38*, 2180–2190.
20. DeShazer, L. G.; Dieke, G. H. *J. Chem. Phys.* **1963**, *38*, 2190–2199.
21. Dieke, G. H.; Pandey, B. *J. Chem. Phys.* **1964**, *41*, 1952–1969.
22. Crosswhite, H. M.; Dieke, G. H.; Carter, W. J. *J. Chem. Phys.* **1965**, *43*, 2047–2054.
23. Dieke, G. H.; Leopold, L. *J. Opt. Soc. Am.* **1957**, *47*, 944–954.
24. Dieke, G. H.; Singh, S. *J. Opt. Soc. Am.* **1956**, *46*, 495–499.
25. Carnall, W. T.; Fields, P. R.; Rajnak, K. *J. Chem. Phys.* **1968**, *49*, 4424–4442.
26. Carnall, W. T.; Fields, P. R.; Rajnak, K. *J. Chem. Phys.* **1968**, *49*, 4450–4455.
27. Carnall, W. T.; Fields, P. R.; Rajnak, K. *J. Chem. Phys.* **1968**, *49*, 4447–4449.
28. Carnall, W. T.; Fields, P. R.; Rajnak, K. *J. Chem. Phys.* **1968**, *49*, 4443–4446.
29. Wybourne, B. G. *Spectroscopic Properties of Rare Earths;* Wiley Interscience: New York, 1965.
30. Görller-Walrand C.; Binnemans K. In: *Handbook on the Physics and Chemistry of Rare Earths;* Karl A. Gschneidner, J. L. E. G. H. L., Choppin, G. R. (eds), **1996**; Vol. 23, p 121–283
31. Carnall W. T. In: *Handbook on the Physics and Chemistry of Rare Earths* **1979**; Vol. 3, pp. 171–208
32. Hellwege K. H.; Orlich E.; Schaack G. *Phys. Kondens. Mater.* **1965**, *4*, 196–206.

33. Pearson J. J.; Herrmann G. F.; Wickersheim K. A.; Buchanan R. A. *Phys. Rev.* **1967**, *159*, 251–261
34. NIelson C. W.; Koster G. F. *Spectroscopic Coefficients for the p^n, d^n and f^n Configurations;* MIT Press: Cambridge, **1963**.
35. Rotenberg M. *3-J and 6-J Symbols;* MIT Press: Cambridge, **1959**.
36. Stark J. *Ann. Phys.* **1914**, *43*, 965–982.
37. Rajnak K.; Wybourne B. G. *J. Chem. Phys.* **1964**, *41*, 565–569
38. Wybourne B. G.; Smentek L. *Optical Spectroscopy of Lanthanides: Magnetic and Hyperfine Interactions;* CRC Press: New York, **2007**.
39. Kramers H. A. *Proc. K. Ned. Akad. Wet.* **1930**, *33*, 959–972.
40. Bünzli J.-C. G.; Eliseeva S. V. *Springer Ser. Fluoresc.* **2011**, *7*, 1–46.
41. Tanner P. A. *Springer Ser. Fluoresc.* **2011**, *7*, 183–234.
42. Liu G.; Jacquier B. (eds) *Spectroscopic Properties of Rare Earths in Optical Materials;* Springer: Heidelberg, **2005**.
43. Sanz J.; Cases R.; Alcala R. *J. Non-Cryst. Solids* **1987**, *93*, 377–386
44. Zeeman P. *Nature* **1897**, *55*, 347.
45. Jørgensen C. K.; Pappalardo R.; Schmidtke H. H. *J. Chem. Phys.* **1963**, *39*, 1422–1430
46. Malta O. L. *Chem. Phys. Lett.* **1982**, *87*, 27–29.
47. Warren K. D. *Inorg. Chem.* **1977**, *16*, 2008–2011.
48. Urland W. *Chem. Phys.* **1976**, *14*, 393–401.
49. Urland W. *Chem. Phys. Lett.* **1978**, *53*, 296–299.
50. Malta O. L. *Chem. Phys. Lett.* **1982**, *88*, 353–356.
51. Albuquerque R. Q.; Rocha G. B.; Malta O. L.; Porcher P. *Chem. Phys. Lett.* **2000**, *331*, 519–525.
52. Jank S.; Reddmann H.; Amberger H. D. *Spectrochim. Acta, Part A* **1998**, *54A*, 1651–1657.
53. Turro N. J.; Ramamurthy V.; Scaiano J. C. *Modern Molecular Photochemistry of Organic Molecules;* University Science Books: Sausalito, **2010**.
54. Cotton F.A. *Chemical Applications of Group Theory;* 3rd edn.; John Wiley & Sons Inc.: New York, **1990**.
55. Walsh B. M. In: *Advances in Spectroscopy for Lasers and Sensing;* Di Bartolo, B., Forte O. (eds); Springer: Dordrecht, **2006**, pp. 403–433.
56. Wybourne B. G. *Mol. Phys.* **2003**, *101*, 899–901
57. Peacock R. D. In: *Structure and Bonding;* Dunitz, J. D., Hemmerich, P., Holm, R. H., Ibers, J. A., Joergensen, K., Neilands, J. B., Reinen, D., Williams, R. J. P. (eds); Springer: Heidelberg, **1975**; Vol. 22.
58. Görller-Walrand C.; Binnemans K. In: *Handbook on the Physics and Chemistry of Rare Earths;* Karl A. Gschneidner, J., Eyring, L. (eds), **1998**; Vol. 25, pp. 101–264.
59. Werts M. H. V.; Jukes R. T. F.; Verhoeven J. W. *Phys. Chem. Chem. Phys.* **2002**, *4*, 1542–1548.
60. Mason S. F.; Peacock R. D.; Stewart B. *Chem. Phys. Lett.* **1974**, *29*, 149–153.
61. Rudzinski C. M.; Engebretson D. S.; Hartmann W. K.; Nocera D. G. *J. Phys. Chem. A* **1998**, *102*, 7442–7446.
62. Hebbink G. A.; Klink S. I.; Grave L.; Oude Alink P. G. B.; Van Veggel F. C. J. M. *ChemPhysChem* **2002**, *3*, 1014–1018.
63. Lamture J. B.; Zhou Z. H.; Kumar A. S.; Wensel T. G. *Inorg. Chem.* **1995**, *34*, 864–869.
64. Nah M.-K.; Cho H.-G.; Kwon H.-J.; Kim Y.-J.; Park C.; Kim H. K.; Kang J.-G. *J. Phys. Chem. A* **2006**, *110*, 10371–10374.
65. Thorne J. R. G.; Rey J. M.; Denning R. G.; Watkins S. E.; Etchells M.; Green M.; Christou V. *J. Phys. Chem. A* **2002**, *106*, 4014–4021.
66. Ha-Thi, M.-H.; Delaire J. A.; Michelet V.; Leray I. *J. Phys. Chem. A* **2010**, *114*, 3264–3269.
67. D'Aleo A.; Pointillart F.; Ouahab L.; Andraud C.; Maury O. *Coord. Chem. Rev.* **2012**, *256*, 1604–1620.

68. Latva M.; Takalo H.; Mukkala V.-M.; Matachescu C.; Rodriguez-Ubis J. C.; Kankare J. *J. Luminescence* **1997**, *75*, 149–169.
69. Yuster P.; Weissman S. I.; *J. Chem. Phys.* **1949**, *17*, 1182–1188.
70. Dexter D. L. *J. Chem. Phys.* **1953**, *21*, 836–850.
71. Förster T. *Ann. Physik* **1948**, *2*, 55–75.
72. Balzani, V.; Campagna, S. (eds) *Photochemistry and Photophysics of Coordination Compounds I., [In: Top Curr. Chem., 2007; 280]*, **2007**.
73. Reinhard, C.; Güdel, H. U., *Inorg. Chem.* **2002**, *41*, 1048–1055.
74. Pope, S. J. A.; Burton-Pye, B. P.; Berridge, R.; Khan, T.; Skabara, P. J.; Faulkner, S. *Dalton Trans*. **2006**, 2907–2912.
75. Lakowicz, J. R. *Principles of Fluorescence Spectroscopy;* Plenum: New York, 1999.
76. Horrocks, W. D. Jr.; Sudnick, D. R. *Acc. Chem. Res.* **1981**, *14*, 384–392.
77. Horrocks, W. D. Jr.; Sudnick, D. R. *J. Am. Chem. Soc.* **1979**, *101*, 334–340.
78. Charbonnière, L. J.; Balsiger, C.; Schenk, K. J.; Bünzli, J.-C. G. *J. Chem. Soc., Dalton Trans.* **1998**, 505–510.